



University of Crete  
Physics Department



FO.R.T.H  
Institute of Electronic  
Structure and Laser

# Development of Terahertz Profilometry Imaging: Application in moisture profilometry

Alexandridi Christina Anastasia

Thesis

For the degree of Master of Science

Heraklion

December 2014



## **Acknowledgments**

Foremost, I would like to express my sincere gratitude to my advisor Prof. Stelios Tzortzakis for the continuous support of my master study and research, for his patience, motivation, enthusiasm, and immense knowledge. His guidance helped me in all the time of research and writing of this thesis. I could not have imagined having a better advisor and mentor for my master study.

Besides my advisor, I would like to thank the rest of my thesis committee: Prof. Dimitris Papazoglou and Prof. Xenophon Zotos for their encouragement, insightful comments, and hard questions.

Furthermore, I would like to especially thank my fellow labmates in UNIS Group, Tasos koulouklidis and Christina Daskalaki for their help and support inside the lab and their guidance in my experimental work. Thanks to their effort and patience, I gained knowledge that helped me with my experimental work during this year. I would also like to thank Michalis Loulakis for his guidance during my first training in the lab. Thanks to him, the maintenance of the laser system made our experimental work easier. In addition, many thanks to Evangelos Marakis for always being cheerful and supportive during both years of my master studies.

Finally, many thanks also to my friends for the great moments we had outside the scientific environment and to my family.

# Contents

<i>Abstract</i> .....	6
<i>Chapter 1: Introduction</i> .....	7
<b>1.1 THz radiation and its characteristic features</b> .....	7
<b>1.2 Applications of THz radiation</b> .....	9
<b>1.3 THz Generation and Detection</b> .....	12
1.3.1 THz sources.....	13
Photoconductive Antennas.....	14
Optical rectification.....	15
Two-color filamentation in air.....	17
1.3.2 THz Detection.....	18
Photoconductive antennas.....	18
Electro-Optic Sampling.....	19
THz Air-Breakdown-Coherent-Detection (ABCD).....	20
<i>Chapter 2: THz Time-Domain Spectroscopy (THz-TDS) and Imaging</i> .....	22
<b>2.1 THz-TDS System (transmission and reflection mode)</b> .....	22
<b>2.2 THz generation: Two-color filamentation in air</b> .....	24
<b>2.3 THz detection: Electro-optic (E.O.) sampling</b> .....	27
<b>2.4 Data Analysis</b> .....	29
2.4.1 Materials' optical characterization in the THz regime.....	29
2.4.2 Extracing information from the Time-Domain and Time-of-Flight Imaging.....	33
<i>Chapter 3: THz Profilometry for Moisture Detection</i> .....	36
<b>3.1 Moisture in Art Conservation and Civil Engineering</b> .....	36
<b>3.2 Demonstration of the THz-TDS reflection system</b> .....	37
<b>3.3 Selection of proper sample material</b> .....	39
<b>3.4 Moisture detection on paper samples</b> .....	41
3.4.1 Sample preparation.....	41
3.4.2 Surface detection and Imaging.....	42
3.3.3 In depth detection and Imaging.....	48
<b>3.4 Moisture detection on gypsum samples</b> .....	52

3.4.1 Sample preparation.....	52
3.4.2 Indepth moisture detection .....	52
<b><i>Conclusions – Perspectives</i></b> .....	<b>58</b>
<b><i>References</i></b> .....	<b>59</b>

## Abstract

Terahertz radiation lies between infrared and millimeter waves in the electromagnetic spectrum. It spans from 0.1 THz to 30 THz and its photons have an energy amount of a few meV. For a long time, this part of the electromagnetic spectrum was known as the “THz gap” due to the lack of coherent sources and detectors. It was only in the late 1980’s when the first demonstration of coherent emission and detection of broadband THz pulses took place and allowed routinely access to this part of the electromagnetic spectrum. Thus, the unique properties of THz radiation have been revealed, suggesting the development of promising applications.

The main characteristics of the THz waves that make them a unique tool for spectroscopic or imaging applications in many scientific fields, from security to applications in medicine and in food industry- are (a) its non-ionizing character due to their low energy (~meV) photons, (b) the fact that many non-metallic and non-polar materials are transparent to THz radiation, due to its long wavelength, (d) are partially reflected from interfaces between non-metallic materials with different refractive indices and (c) the fact that THz radiation is highly absorbed by water.

Due to these properties THz waves can become a very useful and promising tool in fields such as art conservation and civil engineering where a common problem is the presence of moisture in walls. In the case of art conservation the presence of water in depth of some millimeters under a mural painting can be disastrous. THz radiation can provide very useful information: (a) for periodically monitoring the conditions of a fresco in terms of a moisture content map of its surface, (b) for early diagnostics, contributing to the detection of in depth humidity and (c) for giving insight about the absorption dynamics of water (or water-based products) in the areas to be treated during the restoration phase. In the civil engineering field, similar problems arise, where the penetration of water in walls can create cracks/defects and thus decrease the strength of concrete structures. These kind of degradations in buildings can become very dangerous especially in seismogenic regions. Thus, as it has already been mentioned, a tool for early diagnostics of the condition and location of moisture in buildings walls is very useful.

In this thesis, a first attempt to create an experimental routine and the appropriate analysis for the detection and localization of moisture in depth of some millimeters, exploiting THz radiation through a THz-TDS reflection system, is going to be presented. First, the operation of our homemade reflection THz-TDS system and its ability to distinguish different moisture contents for paper samples, with single surface and stratified ones, is demonstrated. Then, a number of different materials are tested in order to choose the most suitable one for our experiments, which we conclude to be the gypsum, a material commonly found in walls. Finally, in the last part of this thesis, the presence and the specific location of moisture is demonstrated both experimentally and theoretically.

# Chapter 1: Introduction

## 1.1 THz radiation and its characteristic features

Terahertz (THz) radiation is the electromagnetic radiation that lies between millimeter and infrared waves in the electromagnetic spectrum. The THz frequency range is typically between 0.1 THz and 30 THz, corresponding to a wavelength range from 3 mm to 10  $\mu\text{m}$ , photon energy from 0.4 meV to 120 meV and to an equivalent black body radiation with temperatures between 4 K and 1200 K as shown in Figure 1.

Being electromagnetic waves, the properties and behavior of THz waves are governed by the Maxwell equations, just like the other waves. However, due to their specific location on the electromagnetic spectrum, THz waves are much more difficult to handle than waves adjacent to them. As a result, technologies in this range have been limited since it is in the upper limit of what is possible with electronics and the lower limit of what is possible with optics. Thus, due to this difficulty of producing strong and dependable sources and efficient detectors in this exotic band of radiation, the THz regime has been for many decades the last part of the electromagnetic spectrum that had not been extensively used for research and technological applications. It is therefore, referred to as the “THz gap”. It was not until the early 80’s that David Auston (at Bell Laboratories) developed the first coherent broadband THz sources as well as coherent THz detectors. Thus, the unique properties of THz radiation have been revealed, suggesting the development of promising applications.

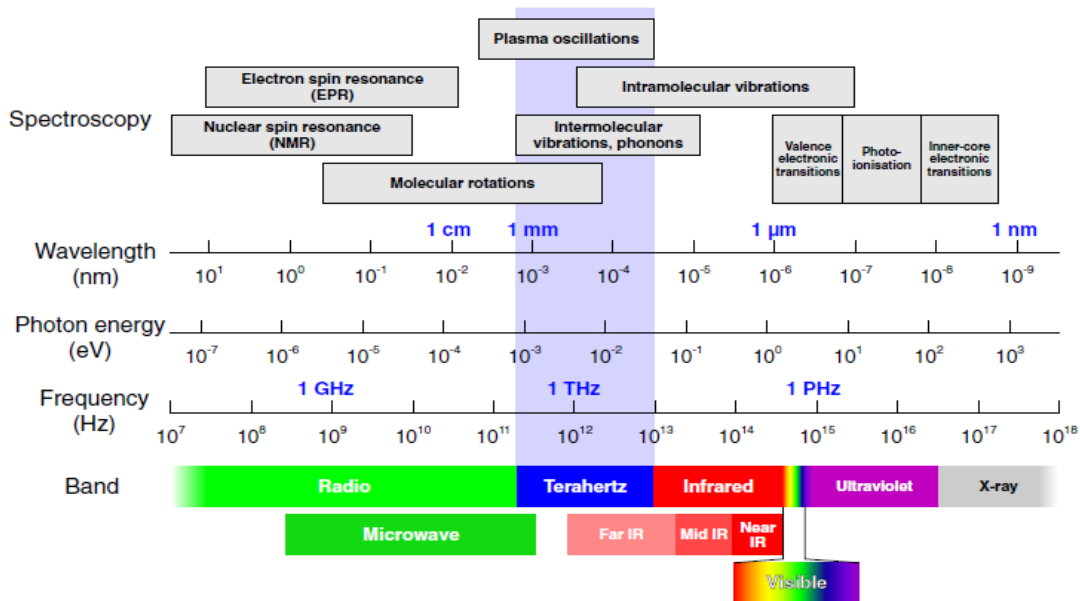
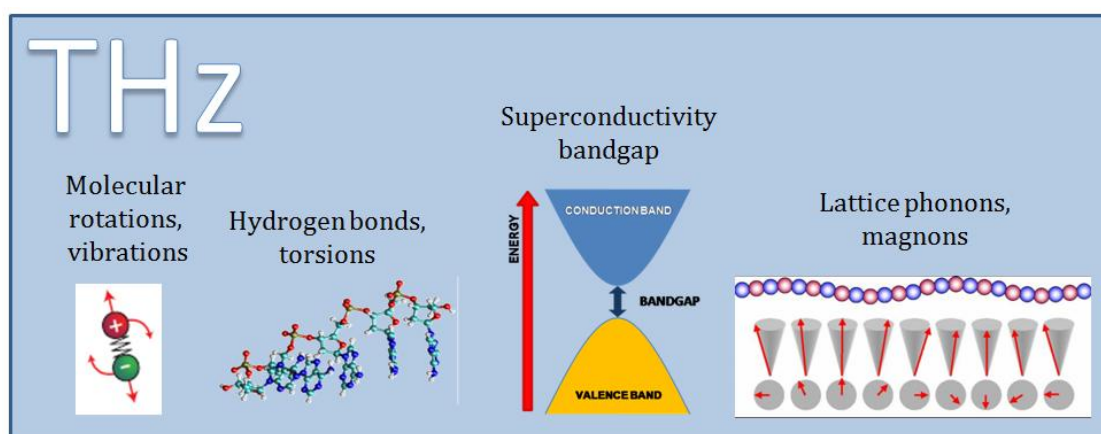


Figure 1: Electromagnetic spectrum from radio to x-ray wavelengths, including spectral ranges for probing different excitations in materials<sup>1</sup>.

THz waves have some really interesting properties that make them a unique tool for research in several scientific fields. First of all, molecular rotations, low frequency bond vibrations and crystalline phonon vibrations are present in this frequency range (see Figure 1 and Figure 2). Thus, many molecules exhibit strong absorption features at the THz frequencies. These transitions are specific to the molecule and therefore enable spectroscopic fingerprinting in the THz range. These unique rotational and vibrational responses of materials provide information that are generally absent in optical, X-ray and nuclear magnetic resonance images such as the identification of substances that are combined of the same atoms only with different structure. In the solid state, also, THz frequencies correspond to the energy scales of phonons, magnons, various particle entities arising from lattice, spin and electronic degrees of freedom. The superconducting gap spans in THz energies for many superconducting materials and the continuous conductivity background in several classes of conductors goes, also, through the THz range. Consequently, THz radiation is a promising tool for fundamental studies and deeper understanding of solid state phenomena.



**Figure 2: Schematic representation of physical phenomena in the THz range.**

Secondly, due to their long wavelength (longer than visible and IR), THz waves are less affected by Mie scattering. That makes them transparent to most dry dielectric materials, such as cloth, paper, wood, and plastic. On the other hand, THz are completely reflected from metallic surfaces and partly reflected from interfaces between dielectric materials with different refractive indices. That enables us to detect objects or defects that are concealed under various surfaces. Thus, THz radiation can be used in industrial control e.g. non-destructive testing<sup>2</sup> and security screening.

Furthermore, the low photon energy of THz radiation (1THz ~ 4.1meV) cannot lead to photoionization in biological tissues in contrast to X-rays. As a result, THz waves are considered safe for both the samples and the operator. Due to the extreme water absorption, THz radiation cannot penetrate into the human body like microwaves can. That allows the use of THz radiation for biological and medical applications but only for limited depth penetration.

Finally, THz pulses can be detected coherently, by the sampling measurement of their electric field, giving a direct access to the amplitude and the phase of the radiation. This gives access to absorption and dispersion spectroscopy of many materials, giving us also chemical and structural information as it is going to be further discussed in Chapter 2.

## 1.2 Applications of THz radiation

THz radiation has been applied to a wide range of research areas, from pure science to industry<sup>3, 4</sup>ENREF2. It is mainly used for spectroscopic studies and imaging applications, while based on the properties discussed above, THz radiation can be applied in communications<sup>5</sup>, astronomy<sup>6, 7</sup>, medical imaging<sup>8-10</sup> and pharmaceutical science<sup>11-14</sup>. Material<sup>15, 16</sup>, chemical<sup>17</sup> and environmental studies, security screening applications<sup>18, 19</sup> and art conservation<sup>20-24</sup> are also scientific fields that THz science finds numerous applications.

The ability of THz waves to characterize the molecular structure of many substances in addition with the transparency of materials used for packaging (paper, plastic, etc.) in the THz region, makes broadband THz time domain spectroscopic (THz-TDS) technique a useful tool for non-invasive control. This can be applied in food industry where numerous THz spectroscopic studies have been made for the detection of antibiotic residues in food<sup>25</sup>. An example is shown in Figure 3(a) where different antibiotics, in various percentages, are mixed with pure honey and have been successfully detected<sup>26</sup>. Figure 3(b) shows also another example, where foreign bodies (a glass splinter, a small stone, and a metal screw), were detected in chocolate bars<sup>27</sup>.

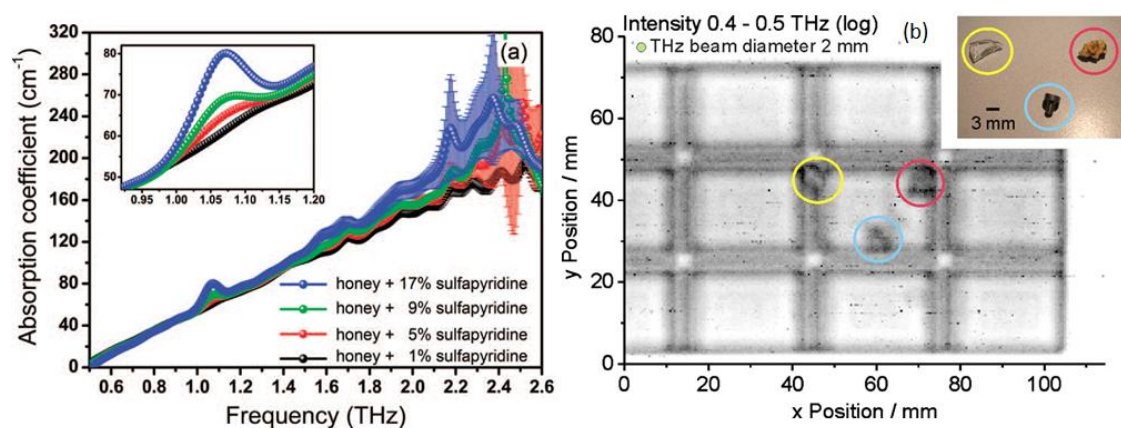
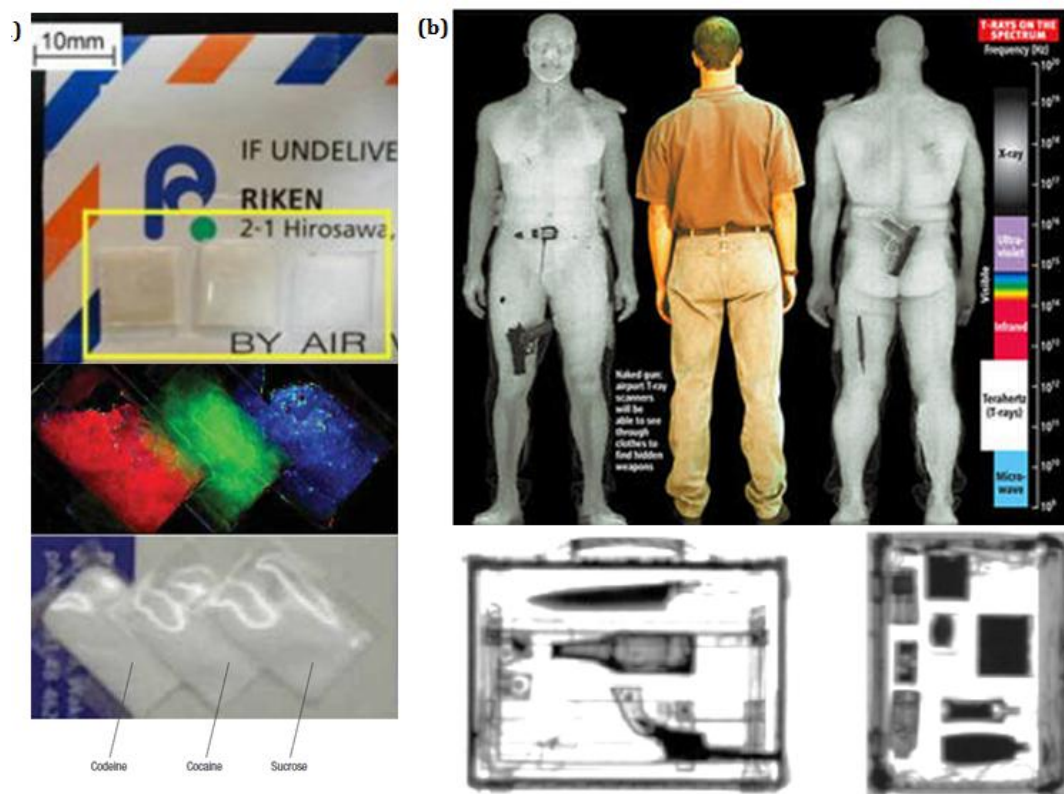


Figure 3: (a) Absorption coefficient of honey mixtures with sulfapyridine antibiotic at different concentrations. Inset: magnified spectral region between 0.9 and 1.2 THz, where the THz fingerprint of sulfapyridine is expected. (b) Photograph inset of three different contaminations and terahertz image of a whole milk chocolate bar, which was contaminated with these types of foreign bodies.

Other promising applications of THz science are found in security industry, where THz waves can be used for imaging the content of postal boxes or envelopes for the detection of drugs and explosives<sup>28, 29</sup> (see Figure 4(a)). Another application is

the THz full body scanners (see Figure 4(b)) that are already available and used in some airports. THz technology can be used as a safe alternative solution for non-invasive imaging of humans, offering the possibility to screen and locate concealed objects or materials due to the non-ionizing nature of THz radiation and the transparency of many materials in this frequency regime.



**Figure 4:** (a) THz spectroscopic imaging of illicit drugs (codeine, cocaine, sucrose) hidden in an envelope. (b) THz body scanner and THz image from the inside of a suitcase.

Another fertile area for the THz science is the pharmaceutical industry. Terahertz pulsed spectroscopy and imaging can be used for on-line physical characterization of pharmaceutical drug materials and final solid dosage forms<sup>30</sup>. THz pulsed spectroscopy can also be used to characterize crystalline properties of drugs and excipients. Different polymorphic forms of a drug can be readily distinguished and quantified. Applications for THz pulsed imaging include the measurement of coating thickness and uniformity in coated pharmaceutical tablets and structural imaging<sup>31</sup>. It is also possible to monitor the hydration or dehydration process of pills throughout the whole process of manufacturing and storage, because water (polar molecule) absorbs strongly THz radiation (see Figure 5).

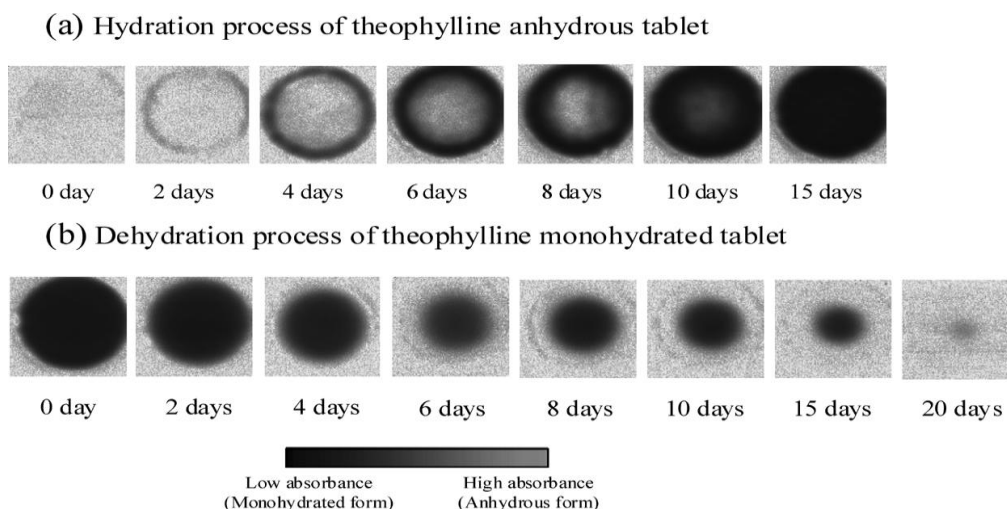


**Figure 5: Chemical mapping of stored theophylline tablets<sup>32</sup>.**

As has been already mentioned, THz radiation is non-ionizing and non-destructive. This property makes THz radiation a very useful tool for medical applications because unlike X-rays, it is harmless for both the samples and the operator. Numerous studies have been carried out on biomolecules, cancer tissues, DNA, proteins and bacteria. For example, it has been reported that hybridized and denatured DNA can be distinguished, so that research can progress towards the development of label-free DNA chips<sup>33</sup>. Other important studies have been made on the diagnosis of cancer<sup>34, 35</sup>. Using THz spectroscopy and imaging, it is possible to distinguish healthy from cancerous tissues, by detecting the different hydration levels between them. Furthermore, skin cancer can be also visualized by the reflection of THz radiation at a lateral and vertical resolution of about 350 $\mu\text{m}$  and 40 $\mu\text{m}$ , respectively, and a penetration depth of about a millimeter can be realized<sup>36, 37</sup>. Finally, THz spectroscopy has been also used for measuring bone density and dental health<sup>38</sup>.

Having a small enough wavelength to permit a spacial resolution down to the sub-millimetre range, but large enough to avoid severe scattering, THz radiation is well adequate for quality control such as monitoring of the drying process of paper in production, giving to the manufacturers valuable informations about the quality of their product<sup>39</sup>. Similar studies have been made for wood<sup>40</sup>, cement and several construction materials. THz science is a powerfull tool, also, for civil engineering<sup>41</sup> where using THz imaging in reflection, defects in parts of buildings such as subsurface cracks on walls<sup>42</sup> can be detected. Even further the usability of pulsed broadband terahertz radiation for the inspection of composite materials from the aeronautics industry have been investigated<sup>43</sup>. A wide range of samples based on glass and carbon fiber reinforced plastics with various types of defects has been examined. Depending on depth, matrix material, and size, defects like foreign material inserts, delamination or moisture contamination can be visualized. If a defect is not too deep in the sample, its location can be correctly identified from the delay between partial reflections at the surface and the defect itself.

THz science has also been successfully applied to the field of art conservation and cultural heritage. Again, due to the non-invasive and non-destructive nature of THz spectroscopy and imaging, they can be used to provide information about the materials existing below the layers of the paint, such as preparation layers, without the need of taking sample from the object. THz spectroscopy is also used for the identification of pigments and binders that exhibit characteristic fingerprints in that frequency range<sup>44</sup> (see Figure 6).

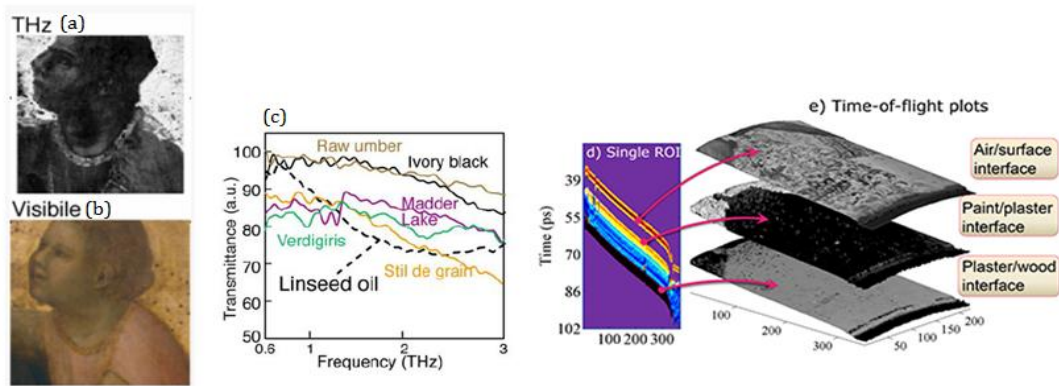


**Figure 6:** Detail from Giotto panel painting courtesy of Uffizi gallery in (a) THz and (b) visible image. (c) Examples of spectra of different pigments and THz images of the different layers of an other painting (d),(e).

Finally, the information and communication technology sector constitutes a large potential market for THz applications. Fibre-linked optical communication is successfully growing, realizing data rates exceeding a terabyte per second, whereas the data rate of wireless communication remains relatively poor. The utilization of THz science would be of great benefit here by enabling high-performance wireless connections<sup>45</sup>.

### 1.3 THz Generation and Detection

Both all-electronic and optoelectronic methods have been developed for the generation and detection of radiation, as well as a small number of THz laser sources as illustrated in table 1. In the present work only the optoelectronic processes are going to be discussed.

	<b>Electronic</b>	<b>Laser</b>	<b>Optical: fs pulse, incoherent multimode, two-colour continuous-wave</b>
<b>Generation</b>	1. Microwave multiplier chain 2. Backward-wave oscillator 3. Gunn diode 4. Resonant tunnel diodes	1. Quantum cascade laser 2. P-type germanium laser 3. Molecule gas laser 4. Free electron laser	1. Photoconductive switch antenna 2. Optical rectification 3. Surface emitter 4. Photo-induced plasma
<b>Detection</b>	1. Schottky diode 2. Backward diode 3. Rectifying transistor (tera-FET) 4. Thermal: Bolometer, Golay cell, pyroelectric, thermopile		1. Photoconductive switch antenna 2. Electro-optic sampling 3. Biased-air detection

**Table 1: Overview of different electronic and opto-electronic THz sources and detectors.**

### 1.3.1 THz sources

In general, optoelectronic THz generation processes exploit the ultrafast intensity modulation of an optical laser source to generate a transient electronic polarization or current on a time scale comparable to or shorter than  $\sim 1\text{ps}$ . The rapid modulation of the polarization  $P(t)$  or the equivalent current  $J(t)=dP/dt$  represents a dipole formation which radiates a new field  $E(t)$  in the THz frequency range (which in the far field follows the relation  $E(t) \propto dJ/dt = d^2P/dt^2$ ).

## Photoconductive Antennas

The use of photoconductive antennas (PCA) or Auston switches is the older and most widely used method for the generation of THz. In this method, a femtosecond laser pulse electrically shortens a biased semiconductor photo-switch. The switch itself consists of a semiconductor material with suitable band gap (GaAs or SoS) and an H-like structure of electrodes (gold or aluminum) with a gap in the order of 5  $\mu\text{m}$  (Figure 7). The electrodes are biased with a voltage of 10 to 50 Volts.

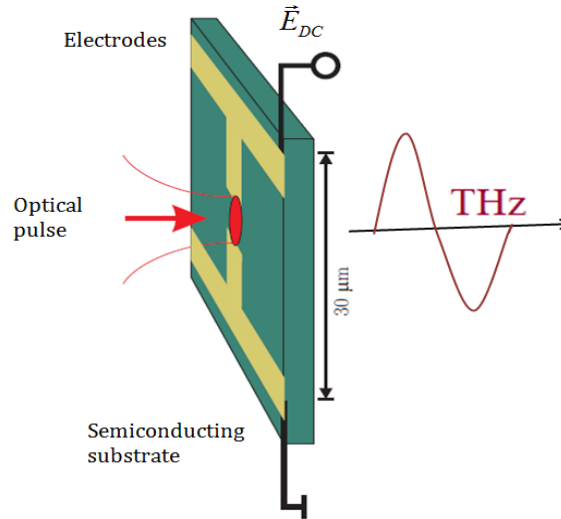


**Figure 7: The Auston switch, consisting of a semiconductor and electric contacts with a gap of the order of micrometers. A femtosecond laser pulse with a wavelength suitable for the band gap of the semiconductor shortens the switch<sup>46</sup>.**

The first step is the optical excitation of the region of high electric field. It is important that the semiconductor bandgap energy is less than the photon energy, so that electron-hole pairs are formed. A focused ultrafast optical pulse incident between the metal lines, generates a thin conductive region. The optically generated electron-hole pairs form an electrically neutral plasma near the semiconductor surface (Figure 8(a)). Then the carriers are accelerated in the applied electric field as shown in Figure 8(b). This spatial separation of the photo-induced electron and hole plasma create a macroscopic polarization,  $P(t)$ , in the semiconductor or an equivalent current density

$$J(t) = N(t)e\mu E_{DC} \quad (1.1)$$

where  $N$  is the density of photocarriers,  $e$  denotes the elementary charge,  $\mu$  is the mobility of electron and  $E_{DC}$  is the bias electric field. The photocarrier density  $N$  is a function of time, whose format is determined by the laser pulse shape and the carrier lifetime. As the photocurrent varies in time, it generates an electromagnetic pulse in the THz region, whose electric field is given by equation (1.2) as shown in Figure 8(d).

$$E_{THz} = \frac{Ae}{4\pi\epsilon_0 c^2 z} \frac{\partial J(t)}{\partial t} \mu E_{DC} \quad (1.2)$$

All these processes happen on time scales of picoseconds or less. On longer time scales, carrier recombination within the semiconductor or at the metal electrodes, causes the induced polarization to decay and the static bias electric field to re-establish itself (Figure 8(e)). The recovery of the semiconductor to its initial state typically takes hundreds of picoseconds or longer.

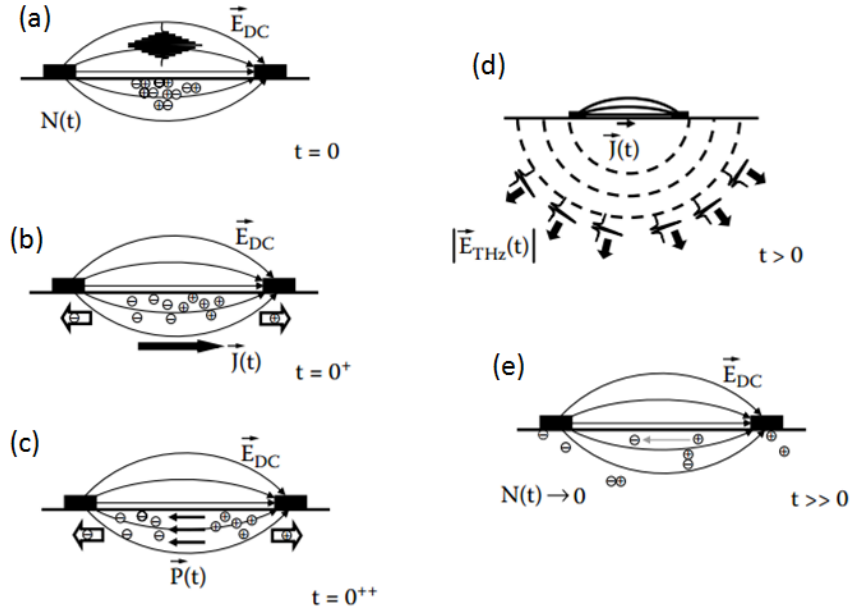


**Figure 8:** Illustration of the process of photoconductive THz generation. (a)The optical pulse generates charge carriers which are accelerated in the static field (b) and create an opposing field in the semiconductor (c). The induced polarization creates a transient current element which radiates a THz pulse (d) followed by recombination back to steady state(e)<sup>47</sup>.

## Optical rectification

In general, when an intense femtosecond laser pulse interacts with matter, electrons are shaken back and forth at the frequency of the light field. When the medium is transparent and exhibits broken inversion symmetry, electrons and ions undergo an additional displacement  $P_r(t)$  as a function of time that roughly follows the intensity envelope of the laser pulse. As this asymmetric or rectified component changes on a timescale of the duration ( $\sim 100$  fs) of the laser pulse, it emits electromagnetic radiation with a bandwidth of  $\sim 1/100$ fs, that is, several THz. This method is commonly used and is known as optical rectification, that is, a process based on the optical response of second order ( $\chi^{(2)}$ ) nonlinear crystals, where due to the asymmetric electron potential in the crystal, the electrons are more easily polarized for one polarity of the optical driving field than the other. This becomes significant

for the strong fields in the fs-pulse. THz generation by optical rectification has the advantage of extremely broad spectral bandwidth.

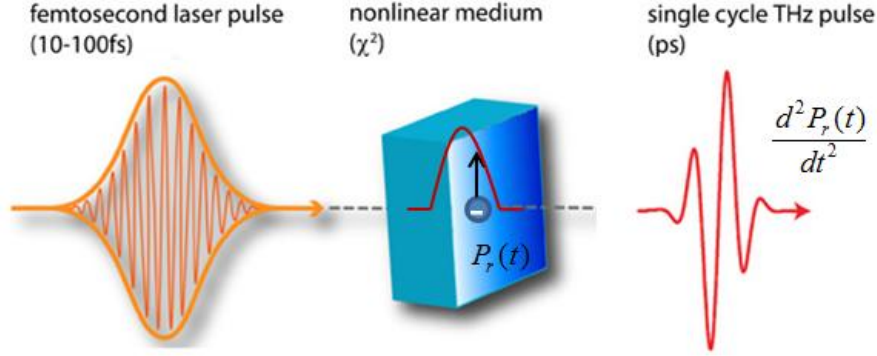


**Figure 9: Schemataion of the generation of a single cycle THz pulse through the optical rectification process.**

The electric polarization of a material is proportional to the applied electric field,  $P=\chi(E)E$ , where  $\chi(E)$  is the electric susceptibility. The nonlinear optical properties of the material are described by expanding  $\chi(E)$  in powers of the field  $E$ <sup>47</sup>

$$P = (\chi_1 + \chi_2 E + \chi_3 E^2 + \chi_4 E^3 + \dots)E. \quad (1.3)$$

Optical rectification is a second order nonlinear optical effect ( $P_2^{nl}$ ) and is described by the  $P_2^{nl} = \chi_2 E^2$  term in the expansion. If we consider the incident light to be a plane wave then  $E$  can be expressed as

$$E(t) = \int_0^{+\infty} E(\omega)e^{-i\omega t} d\omega + c.c. . \quad (1.4)$$

By substituting equation (1.4) in equation (1.3) the polarization for optical rectification is given by

$$P_2^{nl}(t) = 2\chi^{(2)} \int_0^{+\infty} \int_0^{+\infty} E(\omega + \Omega)E^*(\omega)e^{-i\Omega t} d\Omega d\omega, \quad (1.5)$$

where  $\Omega$  is the frequency difference of two optical frequency components. The production of THz radiation relies on this difference frequency generation with the frequency difference close to zero<sup>48</sup>. The bandwidth of the THz radiation pulse is determined by difference frequency generation by all frequencies within the bandwidth of the fs laser pulse. In the far field the radiated electric field is given by equation:

$$E_r(t) \propto \frac{\partial^2 P_2^{nl}(t)}{\partial^2 t} \quad (1.6)$$

It is important to realize that THz currents are triggered throughout the volume of the mixing material (crystal). The radiation emanating from all these local sources has to interfere constructively far from the medium. Therefore, long generation lengths require that the group velocity of the femtosecond pulse equals the THz phase velocity. This is possible only when phase matching is satisfied, which requires conservation of energy and momentum in the nonlinear process. Other factors that affect the radiation efficiency, waveform and frequency distribution are the mixing material itself, the crystal orientation, thickness, absorption and diffraction. The most often-used materials are the inorganic crystals ZnTe and LiNbO<sub>3</sub>.

### Two-color filamentation in air

Another recently established generation method is based on focusing the optical pump beam in a gas medium, where intensities  $I_{\text{opt}} \geq 10^{13} \text{ Wcm}^{-2}$  lead to a significant photoionization of the gas molecules to form a plasma. The same optical pump field then subsequently accelerates the ionized electrons to produce THz polarization. In order to achieve a dipolar polarization one may either add an additional dc bias field to the plasma region (one color filamentation), or more effectively, use a scheme where both the fundamental ( $\omega$ ) IR pulse and its second harmonic ( $2\omega$ ) are overlapped, which results in an asymmetric optical field profile (Figure 10). This two color plasma emitter is particularly attractive in terms of the achievable THz peak fields ( $\geq 1 \text{ MVcm}^{-1}$ ) and bandwidth ( $\geq 10 \text{ THz}$ ). This happens for several reasons. Firstly, there is essentially no damage threshold for plasma formation. The emitting gas medium is intentionally “destroyed”-i.e. ionized- with each laser shot and replenished for the next one. Secondly, there is absence of material absorption or dispersion and finally the photoionization process exhibits an extreme nonlinear response. The generation of THz pulses through two-color photo-induced plasma will be discussed in detail in Chapter 2.

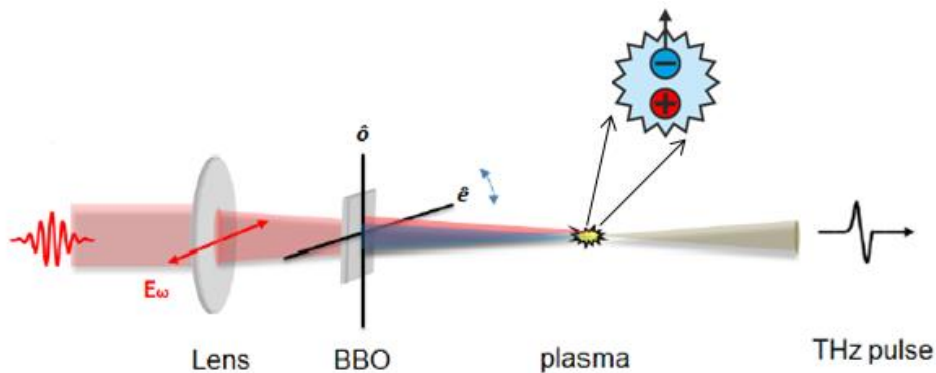


Figure 10: Schematic of all-in-line second harmonic and THz generation<sup>49</sup>.

### 1.3.2 THz Detection

One of the most attractive features of optoelectronic THz spectroscopy is the ability to coherently detect the THz electric field (i.e. both amplitude and phase). This allows not only to determine the absorption and dispersion properties of the samples simultaneously, but also results in a far higher sensitivity/dynamic range compared to square-law (intensity) detection (e.g. with a thermal detector or conventional photodiode). This is because the measured electronic signal amplitude  $S$  is proportional to the THz field amplitude, i.e.  $S \propto E \propto \sqrt{I}$ , as opposed to the intensity ( $S \propto I$ ) in the case of a square-law detector. For fs-pulse systems, one employs the same laser pulses used for generation, which are typically still short compared to the period of the THz wave, and hence can be used as a detection ‘gate’ to sample the THz field as a function of time. Such time-domain sampling is depicted in Figure 11, where the THz and optical detection pulses arrive at the detector with a variable delay ( $\tau$ , controlled using e.g. a mechanical delay line). By scanning  $\tau$  (with an appropriate resolution and range), one obtains a sufficient, discrete representation of the time-domain pulse  $E(t)$ , from which the complex spectral field (amplitude and phase of each spectral component) can be generated by a numerical Fourier transformation.

On the other hand there are also incoherent methods for the detection of THz pulses such as pyroelectric detectors, bolometers, Golay cells. These techniques allow only the signal’s amplitude detection and are broadband detection systems with their main advantage being the relative operation simplicity without the need of adjustment in wide frequency band.

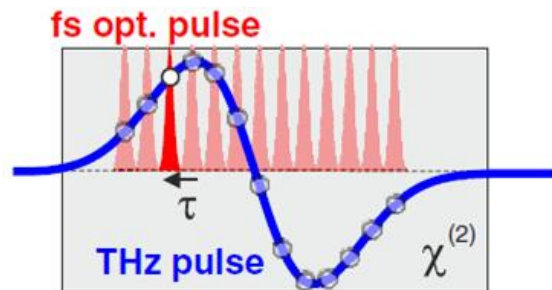
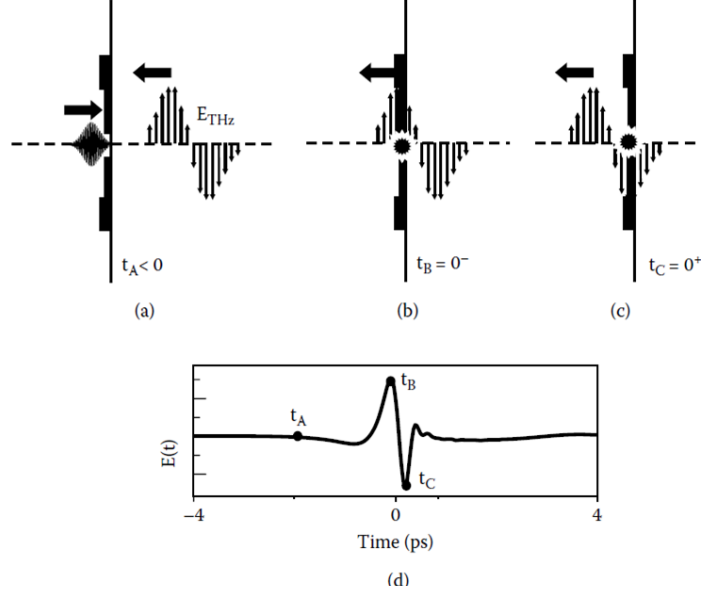


Figure 11: Principle of time-domain sampling of a THz pulse using fs-optical gate pulses as a function of pulse delay  $\tau$ .

### Photoconductive antennas

The principle of the photoconductive method is very similar to the generation discussed in section 1.3.1. The process is illustrated in Figure 12.



**Figure 12: Illustration of the process of THz detection. The electric field measurement is determined by the relative arrival times of the optical and THz pulse. In (a), the optical pulse arrives before the THz pulse. By delaying arrival of the optical pulse to coincide with the THz pulse as shown in (b) and (c), the measured current (d) maps out the THz field in time<sup>47</sup>.**

Figure 12(a) is a side-on view that illustrates the ultrafast laser pulse incident from the left on the antenna. A THz pulse is propagating from the right, but has not yet arrived at the antenna structure. As in generation of THz pulses, the ultrafast laser pulse generates an electron and hole plasma which decreases conductivity of the antenna gap. The time resolved change in conductivity is  $\sigma(t) = N(t)e\mu$ , where  $N(t)$  is the density of photocarriers and  $\mu$  is the semiconductor mobility. The arrival of the laser pulse is analogous to closing a switch, which allows the antenna gap to conduct. The short recombination time  $\tau_c$  of the semiconductor causes the gap resistance to change from nearly insulating to conducting (closing the switch) then back to insulating (opening the switch) on a picosecond time scale. The coplanar strip line is connected to a high-sensitivity current amplifier that detects any current flow through the antenna gap of the order of several hundred pico-amperes up to tens of nano-amperes.

The induced THz field current is  $J(t) = \sigma(t)E(t)$  that is

$$J(t) = N(t)e\mu E(t), \quad (1.7)$$

where  $t$  is the time delay between the fs laser pulse and the incident THz pulse.

## Electro-Optic Sampling

The use of nonlinear ( $\chi(2)$ ) crystals for detection typically employs the electro-optic (EO) or Pockel's effect, where the THz electric field induces an instantaneous birefringence i.e. difference in the refractive indices along each crystal axis, in the

crystal (figure 13). This leads to a change in the polarization state ( $\propto E(t)$ ) of the co-propagating optical detection pulse, which can be detected after the crystal, using a combination of polarization optics and a pair of photodetectors (the use of such ‘balanced’ detection improves the sensitivity by cancelling most of the laser fluctuations). This particular detection method is going to be presented in details in section 2.3.

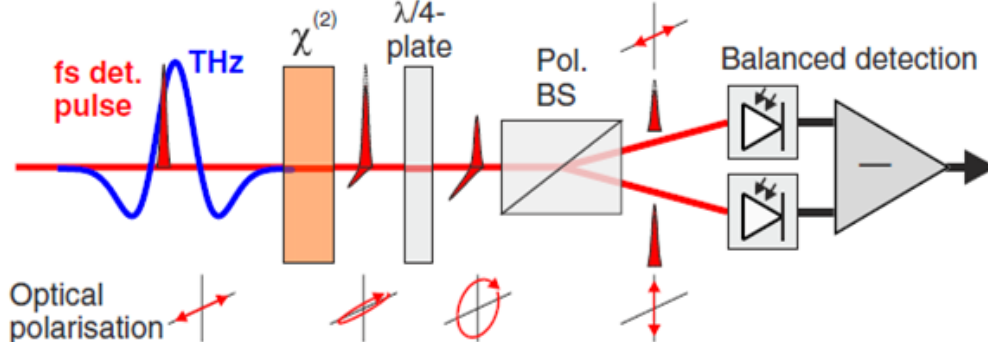


Figure 13: Schematic of electro-optic time-domain sampling utilizing the Pockels effect in nonlinear crystals to transfer the instantaneous THz field onto the polarization of the optical detection pulse with subsequent measurement using polarization optics and a balanced pair of photodetectors<sup>1</sup>.

### THz Air-Breakdown-Coherent-Detection (ABCD)

More recently, detection techniques for fs amplifier lasers have been developed where only a gas medium (e.g. air) is used as the detection medium. The advantages of this particular detection method is that reaches frequencies up to 30 THz and, different from solid state sensors, gaseous media have no phonon resonances (only relatively weak vibrational/rotational resonances in molecular gases) thus, exhibit much lower dispersion and are, also, continuously renewable.

As shown in a typical ABCD set up (Figure 14), the probe beam is sent through a time delay stage and is focused by a lens through a hole in a parabolic mirror. Thus, the THz wave after the interaction with the sample, propagates collinearly with the probe beam and is focused at the same spot. A 500 Hz electric bias field is applied to the detection region, supplying a second harmonic local oscillator. This THz induced second harmonic which is the measured quantity and is generated through a third-order nonlinear process (i.e. two fundamental photons are mixed with a THz photon and create one second harmonic photon, which is also called THz-field-induced second harmonic (TFISH) generation), is passed through a pair of 400 nm bandpass filters and then detected coherently by a photomultiplier tube. The measured second harmonic intensity can be expressed as<sup>50</sup>:

$$I_{2\omega}(\tau) \propto 2[\chi^{(3)} I_{\omega}(t)]^2 E_{bias} E_{THz}(t - \tau) \quad (1.8)$$

The linear dependence of  $I_{2\omega}$  on  $E_{\text{bias}}$  indicates heterodyne detection meaning we get information about both amplitude and phase.

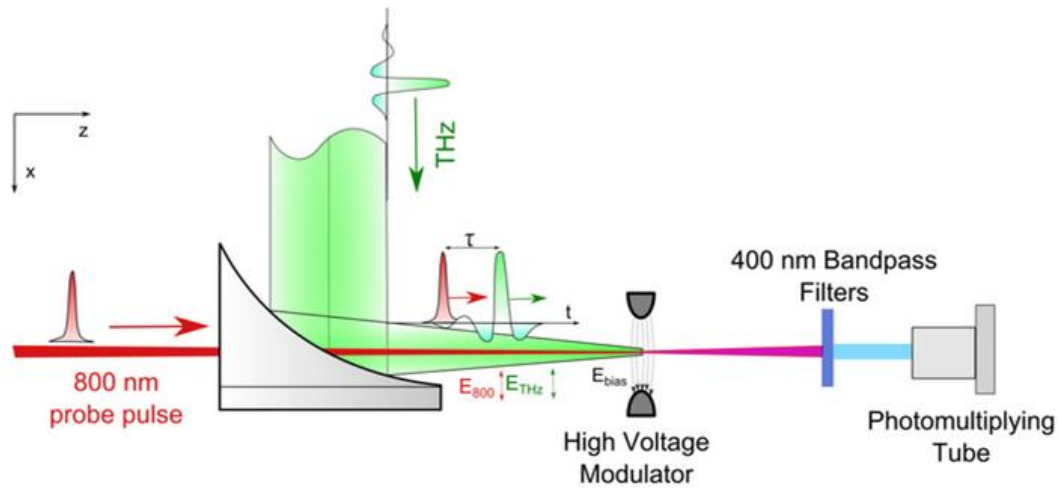


Figure 14: Illustration of a THz- ABCD system.

## Chapter 2: THz Time-Domain Spectroscopy (THz-TDS) and Imaging

### 2.1 THz-TDS System (transmission and reflection mode)

Terahertz time-domain spectroscopy (THz-TDS) is a pump-probe technique, in which the required informations are extracted by shining the sample with a pump pulse -therefore some kind of excitation is generated- and after an adjustable time delay the probe pulse is used to detect coherently the reflection or transmission of the pump beam. Both transmission and reflection THz-TDS systems work under the same principles. However, a reflection setup is more appropriate for samples with high absorption or dispersion, and multilayered samples and it can also be easier introduced in the field for online and in situ operation.

Our homemade THz-TDS system working in transmission mode is illustrated in Figure 15. A powerful amplified kHz Ti:Sa laser system delivering 35 fs pulses at 800 nm central wavelength and energy of 2.3 mJ per pulse is used. The ultrafast laser pulse is first, split into pump and probe beams by a dielectric beam splitter, where the 90% is used for generation of THz pulses and the 10% is used for THz detection. In our system the THz pulses are generated from a two-color filament in air. For this purpose, the pump beam passes through a Beta Barium Borate (BBO) crystal (50 $\mu$ m), generating the second harmonic, before it is focused into air to produce a two-color filament and subsequently THz radiation. After generation, a silicon filter is placed to cut the visible light and to let only the THz pulses pass. Then the THz pulses are collected and focused on the sample with the help of two off-axis parabolic mirrors with gold coating. Another couple of parabolic mirrors is used to collect the transmitted THz pulses from the sample and focus them on the detection system which in our case is the electro-optic sampling<sup>51</sup>. The detection beam travels along a path which has adjustable length, via a delay line. Both detection beam and THz pulses meet on the pellicle beam splitter and then co-propagate collinearly. Changing the delay line's length, the arrival time of the detection pulse is changed with respect to the THz pulse at the detector. When repeating the measurement of the THz field for a set of different delays, the THz waveform is being sampled in its entirety (Figure 11). For the electro-optic detection a 500  $\mu$ m thick Zinc telluride (ZnTe) crystal and a 100  $\mu$ m Gallium phosphide (GaP) crystal is used along with a wollaston prism and a balanced detector to record the difference between s and p polarization parts of the probe beam and thus measure the induced ellipticity. Finally, the whole set up is enclosed in a purged gas chamber to prevent THz absorption from atmospheric humidity.

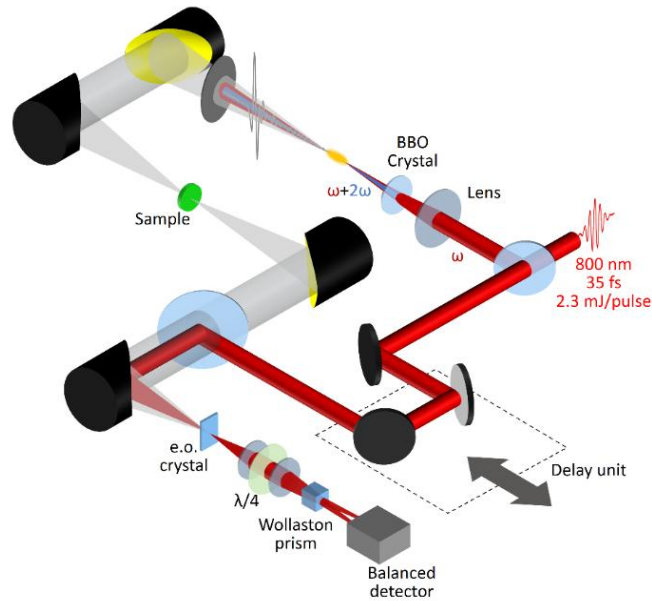


Figure 15: Schematic representation of the THz experimental setup in transmission mode.

In Figure 16, our homemade THz-TDS setup in reflection mode is illustrated. This is the main setup which was used for this thesis. The principles are exactly the same as in the case of the transmission mode of the setup. The main difference is that the THz waves hit the sample, which is mounted on a metallic surface on an X-Y-Z translation stage, in an incident angle of  $\theta=30^\circ$  and the collected radiation is the one that is reflected from the sample. For the electro-optic detection in this setup was used only the ZnTe crystal.

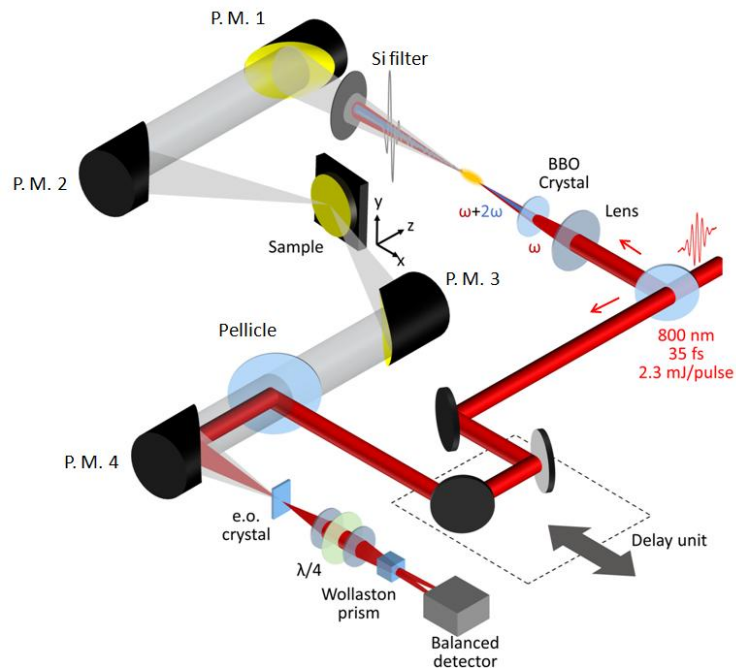


Figure 16: Schematic representation of the THz experimental setup in reflection mode. P.M.1 and P.M.4 are in a  $\theta=90^\circ$  angle and P.M.2 and P.M.3 in a  $\theta=30^\circ$  angle (P.M. = Parabolic Mirror).

## 2.2 THz generation: Two-color filamentation in air

When the fs-laser beam is focused on air, a plasma filament is formed. This process can be described as a self-action process, in which an intense ultrashort laser pulse undergoes strong spatial and temporal reshaping as it propagates in a transparent medium. It results in the propagation of the beam with a very narrow waist that remains almost constant over many Rayleigh lengths, leaving ionized channels in its wake. This phenomenon is the result of a competition involving linear and highly nonlinear effects, such as the optical Kerr effect, defocusing due to plasma created by optical field ionization, nonlinear losses, dispersion, and others<sup>52</sup>.

Recently, THz generation via two-color laser filament in air has attracted a considerable amount of interest due to its capability of producing broadband and high-power THz pulses. The use of air (or selected gases) as the THz wave emitter provides superior bandwidth covering the entire THz gap and well beyond, extremely high THz electric fields, which are comparable to those obtained with large-scale facilities, only accessible in some national laboratories<sup>53</sup>, and standoff sensing capability in atmosphere, which was considered nearly impossible due to the high-atmospheric moisture attenuation in the THz frequency range. THz air photonics provides a spectral range covering from 0.2 THz to over 30 THz, which is only limited by the optical pulse duration without suffering from the phonon absorption and significant dispersion in semiconductors and nonlinear crystals.

The experimental set up is shown in Figure 10. An ultrashort pulsed laser beam ( $\omega$ ) and its second harmonic ( $2\omega$ ) - which is generated after introducing a frequency doubling crystal (BBO, b-barium borate) prior to the formation of the plasma string - are co-focused in air to ionize air molecules. From the laser-ionized plasma, strong THz pulse emission is observed. The physical mechanism of the THz emission in gas plasma has been under debate for quite long time. There are typically two models used to explain the nonlinear optical processes responsible for the THz generation in gas plasma which are the four wave rectification (FWR) model and the asymmetric transient current (ATC) model.

Firstly, the FWR model was introduced about a decade ago by Cook and Hochstrasser<sup>54</sup> and it is based on a macroscopic third order ( $\chi^{(3)}$ ) nonlinear interaction between the ( $\omega$ ) and ( $2\omega$ ) waves. In a FWR process, the carrier frequencies of three input fields add to zero, and the nonlinear response is driven by the product of the field envelopes of the input pulses. In one possible mechanism for FWR, the nonlinear polarization induced by the input waves acts as the source of the THz radiation. This process is schematically represented in Figure 17 for a multi-cycle two-color pulse.

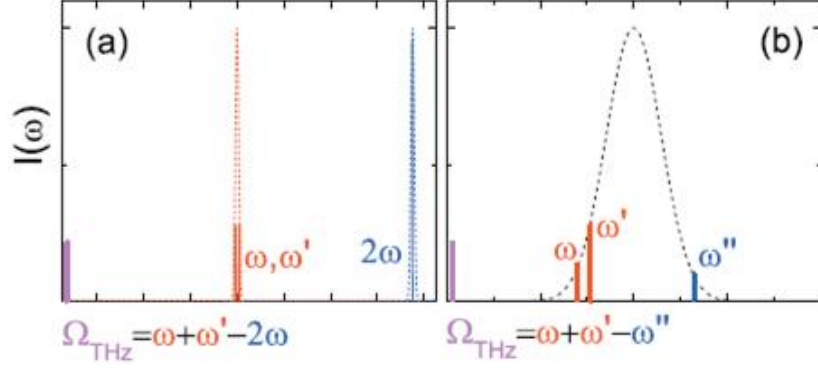


Figure 17: Schematic of generated THz spectra in a four-wave rectification for (a) the AC-bias ( $\omega$ - $2\omega$ ) method with multicycle pulses and (b) few-cycle pulses<sup>55</sup>.

For the first case, the emitted THz electric field can be expressed as:

$$E_{THz}(t) \propto \chi^{(3)} E_{2\omega}(t) E_{\omega}^*(t) E_{\omega}^*(t) \cos(\varphi) \quad (2.1)$$

and for low input laser power, equation (2.1) becomes<sup>56</sup>:

$$E_{THz}(t) \propto \chi^{(3)} \sqrt{I_{2\omega} I_{\omega}} \cos(\varphi). \quad (2.2)$$

The second model, suggests that the emission of THz pulses from a 2-color filament is the result of a transversal photocurrent<sup>57</sup>. When the fundamental ( $\omega$ ) and the second harmonic ( $2\omega$ ) laser beams are combined, they result in a symmetry-broken laser field. With both ( $\omega$ ) and ( $2\omega$ ) linearly polarized, the total laser field is given by equation:

$$E_L(t) = E_1 \cos(\omega t + \varphi) + E_2 \cos[2(\omega t + \varphi) + \theta] \quad (2.3)$$

where  $E_1$  and  $E_2$  are the amplitudes of the fundamental ( $\omega$ ) and the second harmonic ( $2\omega$ ) fields, and  $\theta$  is the relative phase between the ( $\omega$ ) and ( $2\omega$ ) fields. It is assumed that the bound electrons of atoms under study are liberated at a phase  $\varphi$  via photoionization. Figure 18(a) shows a combined electric field of ( $\omega$ ) ( $\lambda = 800$  nm) and ( $2\omega$ ) ( $\lambda = 400$  nm) for a relative phase of  $\theta = 0$  and  $\theta = \pi/2$ . Figure 18(b) shows the trajectories of electrons born at various phases of  $\varphi = -9\pi/10, -\pi/10, \pi/10,$  and  $9\pi/10$  with respect to the fundamental laser field (for both  $\theta = 0$  and  $\theta = \pi/2$ ). Once bound electrons are liberated via ionization, the electron trajectories and velocities are calculated by:

$$v_d = \frac{eE_1 \sin \varphi}{m_e \omega} + \frac{eE_2 \sin(2\varphi + \theta)}{2m_e \omega} \quad (2.4)$$

where  $m_e$  is the electron mass. As shown in figure 18(b), with even-function symmetry ( $\theta = 0$ ), the drift velocity cancels for electrons born at opposite laser field

slopes. With  $\theta = \pi/2$ , however, there is a non-vanishing drift velocity in the positive direction. The drift velocity for all  $\phi$  is plotted in Figure 18(c) for  $\theta = 0$  and  $\theta = \pi/2$ , along with the corresponding laser field (dotted line). Since the ionization occurs near the peak of the laser field, only the shadowed area of the electron drift velocity contributes to the overall electron current. In contrast to the  $\theta = 0$  case, there is a net electron current with  $\theta = \pi/2$ , and this, with a time-varying electron density over the entire laser field envelope, produces a current surge which emits THz radiation. This net current is given by equation:

$$J_{\perp}(t) = \int_{t_0}^t e v_e(t, t') N_e(t) dt' \quad (2.5)$$

where  $N_e$  is the electron density calculated from the ionization rate, and the corresponding THz electric field is given by equation:

$$E_{THz} \propto \frac{dJ_{\perp}(t)}{dt} = e \frac{dN_e(t)}{dt} v_{d(t)} \quad (2.6)$$

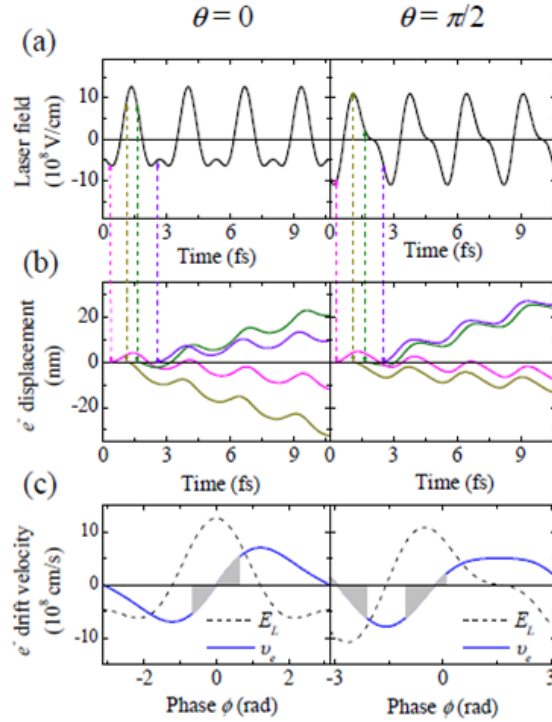


**Figure 18:** (a) Laser fields with the fundamental and second harmonic with a relative phase  $\theta = 0$  and  $\pi/2$ . (b) Electron trajectories born at various phases of  $\phi = -9\pi/10, -\pi/10, \pi/10,$  and  $9\pi/10$ . (c) Drift electron velocity versus  $\phi$  (solid line), overlaid with the laser field (dashed line)<sup>57</sup>.

## 2.3 THz detection: Electro-optic (E.O.) sampling

Electro-optic sampling is a coherent optoelectronic technique of optical sampling in which the propagation of THz waves through optically active crystals leads to the linear electro-optic effect or Pockels effect, which is the basis of electro-optic detection techniques. In electro-optic sampling, the THz electric field is measured by modulating an optical probe pulse inside an electro-optic (e.o.) crystal, where it changes the polarization ellipsoid of its refractive index. The linearly polarized probe pulse copropagates inside the crystal with the THz pulse (pump), and its phase is modulated by the refractive index change. The existence of the THz field changes the birefringence of the electro-optic crystal, causing the refractive index difference for polarizations along different axes of the crystal. This polarization change is converted to intensity change by an analyzer, for example a Wollaston prism. Usually a pair of balanced photodiodes is used to suppress the common laser noise while the signal is doubled.

In order to measure this phase delay, we can use a balanced detection. In Figure 19 the process of balanced measurement is represented. A linearly polarized probe beam is modified to elliptical polarization through the electro-optic process. A quarter-wave plate is used to bias the polarization of the probe beam. An analyzer (Wollaston prism) is used to split the biased probe beam into s and p polarization components and a pair of balanced photodetectors is used to measure the difference between them. When no THz field is applied, s and p polarization components will have the same intensity after the analyzer and the balanced detector gives no signal. The presence of a THz electric field changes the polarization of the probe beam, generating a measurable signal in the balance detector which is:

$$S \propto \sin \Gamma \quad (2.7)$$

where  $\Gamma = \frac{2\pi d}{\lambda} \Delta n$ , is the relative phase delay between the components of the laser beam after entering the electro-optic crystal.

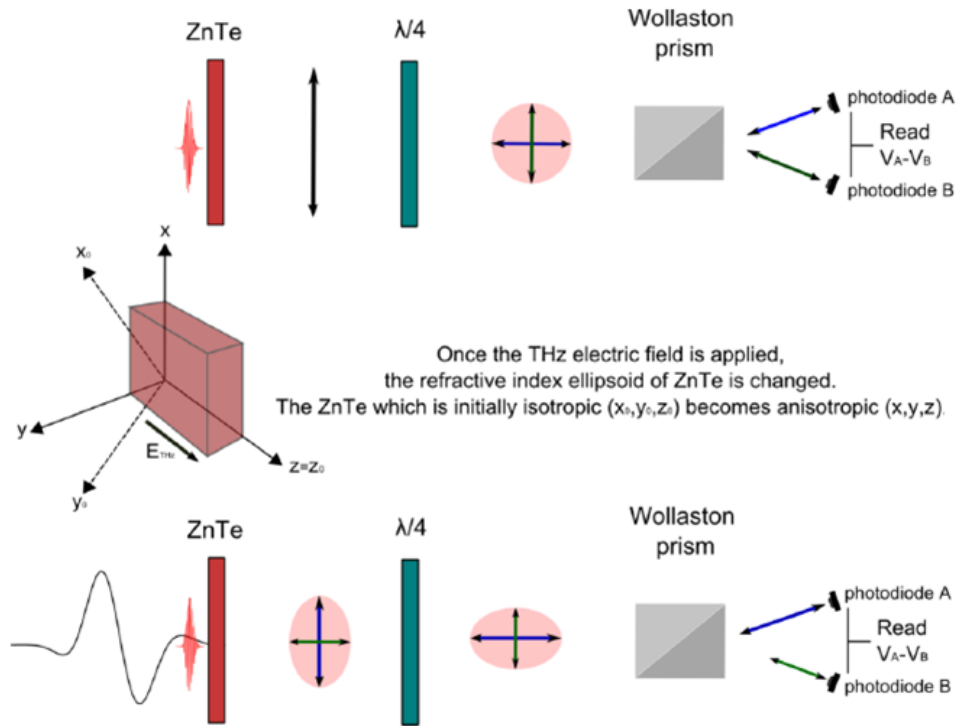


**Figure 19: Schematic representation of a balanced electro-optic set-up.**

The measurement of the THz electric field is performed by the aid of a lock-in amplifier. This device selectively amplifies the incoming signal in order to boost it above the noise level. To measure the entire THz waveform, a standard optical sampling is performed as follows. Owing to the periodicity of the laser pulses, we can use a pump probe method to measure the entire THz waveform. By changing the distance between the THz pulse and the optical probe pulse with an optical delay line, one can change the time delay between these two pulses and map the electric field of the THz pulse, representing the temporal evolution of the pulse electric field. A schematic representation of the  $E(t)$  recorded THz signal at each different time delay is shown in Figure 20.

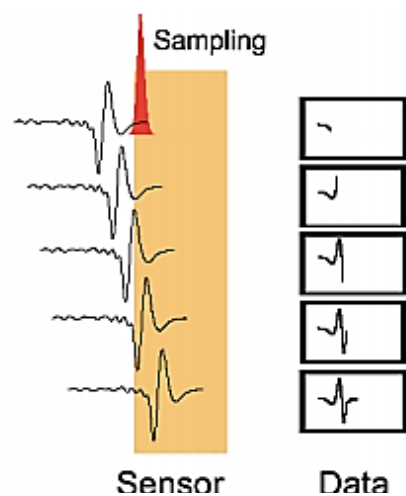


**Figure 20: The measurement of the entire THz waveform.**

## 2.4 Data Analysis

### 2.4.1 Materials' optical characterization in the THz regime

In a pulsed THz system, the waveform of the THz pulse  $E(t)$  represents the temporal evolution of the pulse electric field. The Fourier transform of the temporal waveform  $E(t)$  gives the spectral distribution of the THz pulse in the frequency domain. The THz electric field in the frequency domain is in principle a complex value containing both amplitude and phase information:

$$\tilde{E}(\omega) \equiv A(\omega)e^{-i\phi(\omega)} = \int dt E(t)e^{-i\omega t} \quad (2.8)$$

The temporal evolution of the electric field of the THz pulse in transmission mode is shown in Figure 21 (a) and Figure 21 (c) as function of the time delay of the probe pulse, using two of the most common electro-optic crystals, a 500  $\mu\text{m}$  thick ZnTe and a 100  $\mu\text{m}$  thick GaP crystal respectively. After Fourier transform, the corresponding amplitude spectrum is obtained and is presented in Figure 21 (b) and Figure 21 (d). Respectively, the temporal evolution of the electric field of the THz pulse in reflection mode is shown in Figure 22 (a) with the corresponding amplitude spectrum in Figure 22 (b), using a 1 mm thick ZnTe crystal for the detection. Two main factors limit the bandwidth of THz radiation in electro-optic sampling is the pulse duration of the excitation laser pulse and phase matching conditions. Roughly speaking, a laser pulse can generate a THz pulse with bandwidth twice that of the laser pulse bandwidth. Therefore, for laser pulse duration of 35fs; the bandwidth is estimated to be above 60 THz. The limiting factor continues to be proper phase matching. Because the frequency extent of the THz pulses is so broad, it is practically impossible to select an electro-optic material that fulfills phase matching requirements for all frequency components. For this reason, using the ZnTe crystal we can detect within a frequency range reaching up to 3 THz while with a GaP crystal the spectral bandwidth is expanding up to 8 THz.

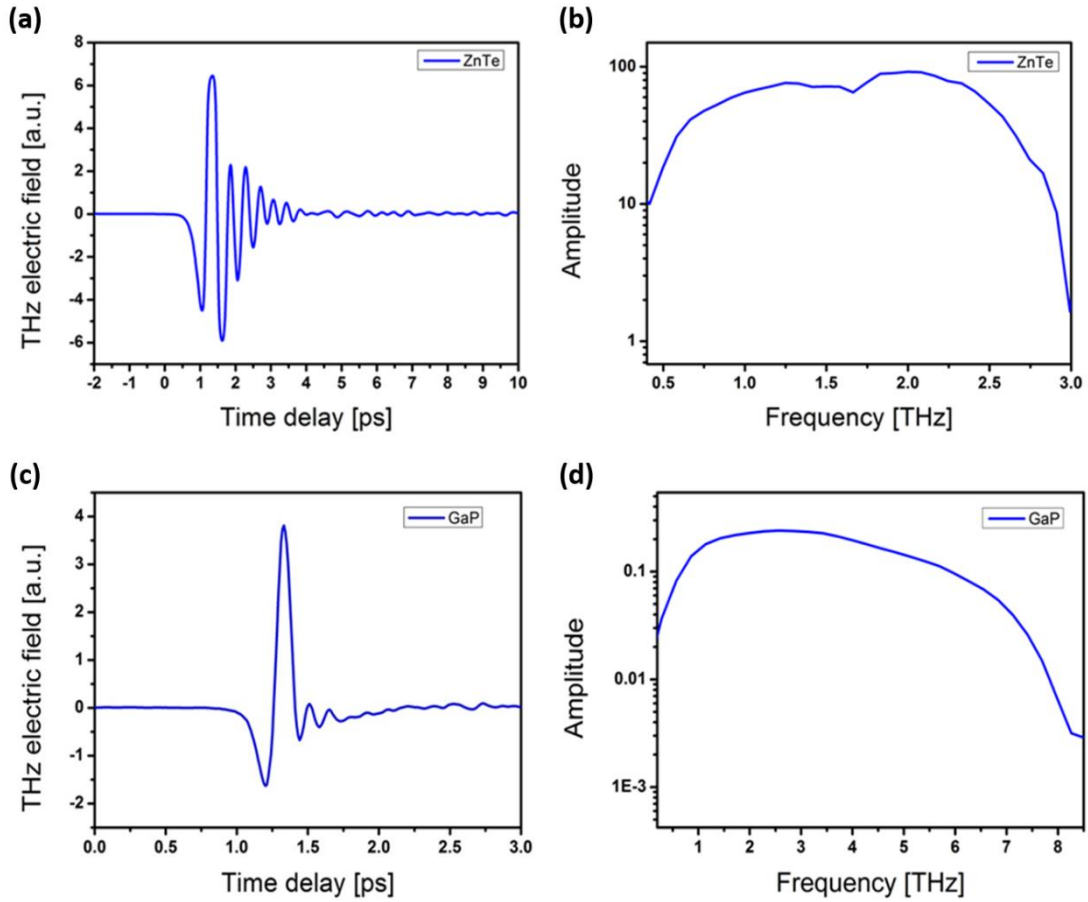


Figure 21: (a) Measured transmitted THz electric field with 500  $\mu\text{m}$  ZnTe crystal and (b) its spectral amplitude. (c) Measured THz electric field with 100  $\mu\text{m}$  GaP crystal and (d) its spectral amplitude.

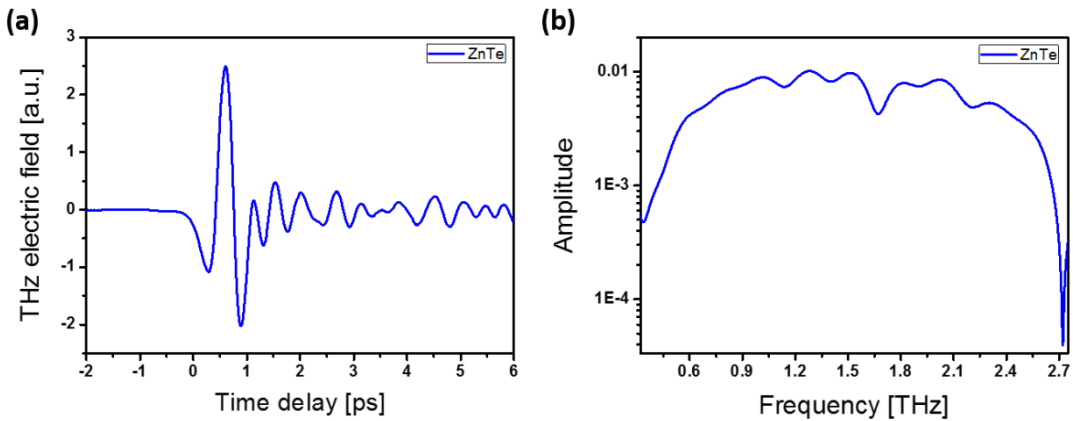


Figure 22: (a) Measured reflected THz electric field with 1mm ZnTe crystal and (b) its spectral amplitude.

The spectral resolution of a THz-TDS measurement,  $\delta\omega$ , is determined by the temporal scanning range  $T$ . The frequency range of the spectrometer is limited by the response of the THz source and detector, while mathematically the spectrum is significant within a bandwidth  $\Delta\Omega$ , which is related to the temporal sampling interval  $\delta t$ . In general the bandwidth and spectral resolution of a THz-TDS are given by:

$$\delta\omega = \frac{2\pi}{T}, \Delta\Omega = \frac{2\pi}{\delta t} . \quad (2.9)$$

When a fast Fourier transform is used, the spectrum is symmetric around  $\Omega=0$ . Therefore, the frequency range spans from  $-1/(2\Omega)$  to  $1/(2\Omega)$ . In order to have a smooth calculated THz spectrum, the zero-padding technique may be applied. The zero-padding method adds several zero values on one side or both sides of the THz waveform. Padding with zero's mathematically increases the temporal scanning range  $T$ , and thus gives more data points in the THz spectrum. However, padding with zero's does not provide any additional information and does not improve the spectral resolution.

To measure the spectral response of a target, one should first record the THz waveform of a reference sample, i.e. free space. The THz waveform of the reference sample is called the reference waveform. The THz waveform transmitted/reflected from the target is called the signal waveform. Fourier transform of the reference and signal waveforms gives the reference spectrum,  $A_R(\omega)e^{-i\phi_R(\omega)}$  and the signal spectrum,  $A_S(\omega)e^{-i\phi_S(\omega)}$ , respectively<sup>58</sup>. The spectral properties of a sample of known thickness  $d$  can be extracted by comparing the signal spectrum with the reference spectrum.

There are some differences in the formulas between transmission and reflection THz-TDS due to the different geometric configuration of the two systems. Thus for the transmission configuration the absorption coefficient is expressed as:

$$a = \frac{1}{d} \ln \left( \frac{A_R(\omega)}{A_S(\omega)} T \right) \quad (2.10)$$

where  $T$  is the Fresnel reflection coefficient for normal incidence:

$$T = \frac{(n(\omega) + 1)^2}{4n(\omega)} \quad (2.11)$$

and the refractive index  $n$  is equal to:

$$n = 1 + \frac{[\varphi_S(\omega) - \varphi_R(\omega)]c}{d\omega} \quad (2.12)$$

Then we know, that the complex permittivity is related to the complex refractive index by the following expression:

$$\begin{aligned} \hat{\varepsilon} &= \hat{n}^2 \\ \hat{n} &= n + ik \end{aligned} \quad (2.13)$$

and where  $k$  is the extinction coefficient equal to:

$$k = \frac{\lambda\alpha}{4\pi} = \frac{c\alpha}{2\omega} \quad (2.14)$$

Hence, the real and imaginary part of the permittivity can be extracted and defined as function of the frequency:

$$\begin{aligned} \varepsilon' &= n^2 - k^2 \\ \varepsilon'' &= 2nk \end{aligned} \quad (2.15)$$

In the case of reflection geometry, the reference signal typically consists of the THz pulse reflected from a mirror surface with a reflection coefficient close to minus unity. The sample signal consists of the THz pulse reflected from the plane sample surface, positioned at the same plane as the reference surface. In this case, the formulas for the absorption coefficient and the refractive index are modified as is shown below.

First we assume normal incidence with a metal mirror as a reference surface. In the frequency domain the ratio between the sample and the reference spectra is then

$$|r|e^{i\phi} = \frac{\hat{n}-1}{\hat{n}+1} = \frac{n+i\kappa-1}{n+i\kappa+1} \quad (2.16)$$

Equation (2.16) can be inverted and simple expressions of the index of refraction and the absorption coefficient can be found<sup>59</sup>:

$$n = \frac{1-|r|^2}{1+|r|^2-2|r|\cos\varphi} \quad (2.17)$$

$$\alpha = \frac{4\pi\nu}{c} \frac{2|r|\sin\varphi}{1+|r|^2-2|r|\cos\varphi} \quad (2.18)$$

If we take into account that THz pulses are incident on the sample under an angle  $\theta$  the analysis gets more complicated. For the reflection coefficient, we get:

$$r = \frac{A_s}{A_R} \frac{n^2-1}{\left(\cos\theta + \sqrt{n^2 - \sin^2\theta}\right)} e^{i\varphi} \quad (2.19)$$

and for the complex index of refraction:

$$\hat{n} = \frac{\sqrt{(1-r)^2 n^2 + 4r \sin^2 \theta}}{r} \quad (2.20)$$

## 2.4.2 Extracing information from the Time-Domain and Time-of-Flight Imaging

Many useful informations can also be extracted directly from the THz electric field. An electromagnetic wave, and in our case THz waves, experience partial transmittance and partial reflectance when the medium through which they travel suddenly changes. Or in other words, when there is a change in the refractive index i.e. the presence of an interface as is illustrated in Figure 23 below from our experimental data.

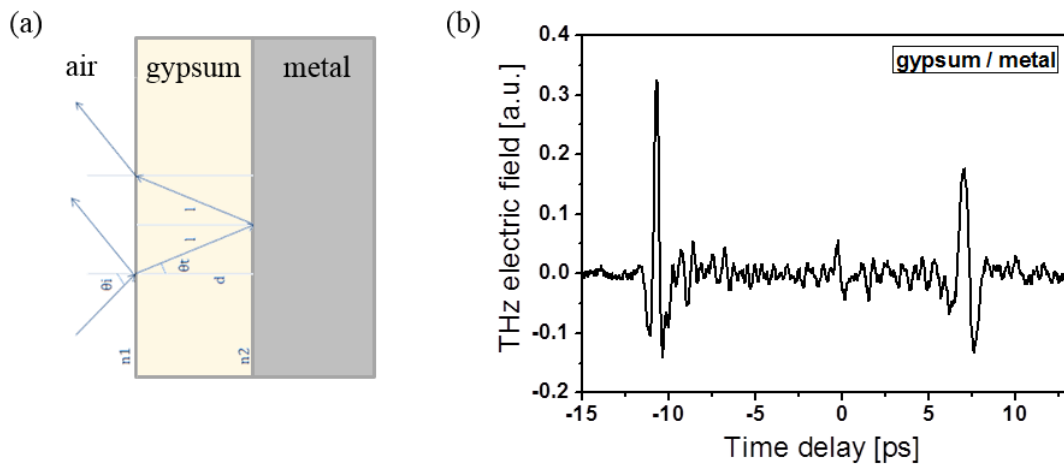


Figure 23: (a) Stratified sample consisting of a first layer of an 1.56 mm thick gypsum and a second layer of a metallic surface. (b) Reflection THz electric field from the stratified sample.

The reflection peaks in a THz electric field can give us information for the exact position of the interface. For this reason, we can consider a two-layer system, as shown in the following figure.

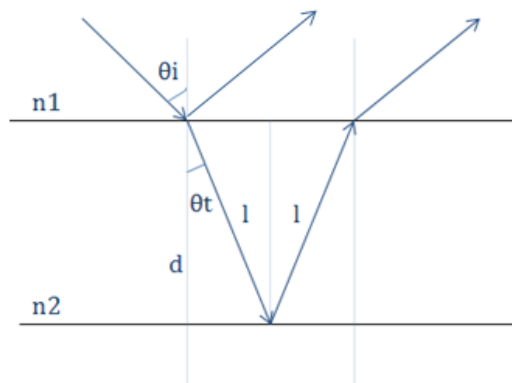


Figure 24: A two-layer system of thickness  $d$ .

For the refractive indices of the two media  $n_1$  and  $n_2$  ( $n_1 \neq n_2$ ),  $\theta_i$  and  $\theta_t$  the incidence angle and the angle of the transmitted beam respectively ( $\theta_i > \theta_t$  when  $n_1 < n_2$ ),  $l$  the distance that light travels from the first interface to the second and  $d$  the thickness of the medium with  $n_2$ , one can say that:

$$c = \frac{x}{t} \Rightarrow \frac{c_0}{n_2} = \frac{2l}{\Delta t} \Rightarrow l = \frac{c_0 \Delta t}{2n_2} \quad (2.21)$$

where  $x = 2l$  is the total path length that is propagated by the portion of the THz beam refracted at the two interfaces,  $n_2 = \frac{c_0}{c}$  is the refractive index of the second medium and  $\Delta t$  the time needed for the THz beam to travel the distance  $x$ .  $\Delta t$  is obtained directly from the recorded THz electric field and is  $\Delta t = |t_1 - t_2|$ , with  $t_1$  and  $t_2$  the arrival times obtained from the positions of the reflection peaks and correspond to the maximum positive THz signal intensity (see Figure 23).

From trigonometry :

$$\cos \theta_t = \frac{d}{l} \Rightarrow d = l \cos \theta_t \quad (2.22)$$

and using Snell's law :

$$n_1 \sin \theta_i = n_2 \sin \theta_t \Rightarrow \theta_t = \sin^{-1} \left( \frac{n_1}{n_2} \sin(\theta_i) \right) \quad (2.23)$$

Finally combining equations (2.21), (2.22) and (2.23) one can find the position of the interface :

$$d = \frac{c_0 \Delta t}{2n_2} \cdot \cos \left[ \sin^{-1} \left( \frac{n_1}{n_2} \sin(\theta_i) \right) \right] \quad (2.24)$$

The above analysis explains the principles on which the time-of-flight imaging is based. In the case of two THz pulses reflected from two surfaces that are located at different depths, the reflected THz pulses have different time delays due to different optical paths. From the time delay, one can retrieve depth information of each pixel, and thus present a tomographic profile of the target. The actual depth resolution that can be experimentally extracted is usually shorter than the THz central wavelength. When THz pulses with a central wavelength at 2 THz are used, the smallest depth resolution can be a few microns.

For the analysis of our measurements, a Labview program was developed in order to automate the acquisition of multiple scans and reconstruction of the measured image. The depth resolution was limited by the wavelength size which is around 300

$\mu\text{m}$  while the spatial resolution by the size of the beam at the THz focus which is around  $800\ \mu\text{m}$ . The THz electric field at different points of the sample in X-Y plane, is recorded. For the analysis of the recorded data, we can choose different options such as to find each maximum peak, the maximum peak to minimum peak distance or we can even use integration of the THz electric field. These options can be applied to the entire electric field or we can choose a particular part of it by an adjustable time window. Each value is then placed in a matrix in correspondence with its position in X-Y space and the image is reconstructed. The highest and lowest values are identified in order to establish the upper and lower limit of the color pallet. In our case red correspond to the highest and blue to the lowest values.

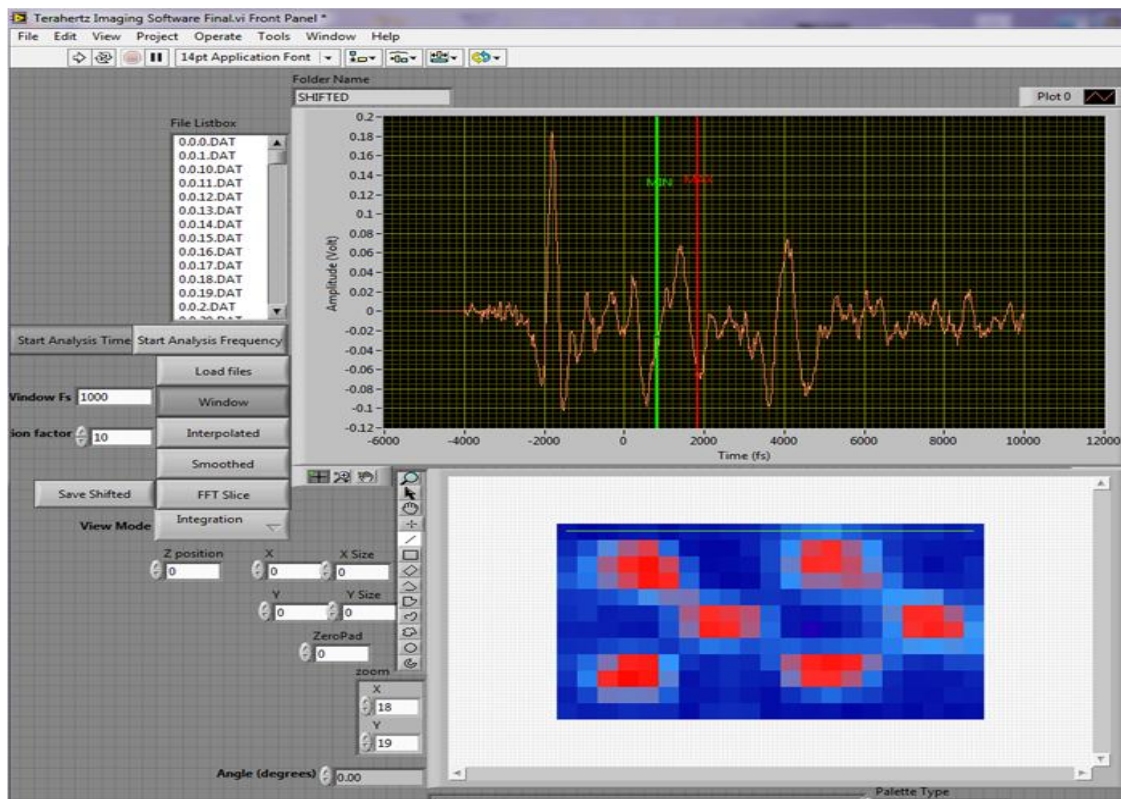


Figure 25: Imaging program in Labview.

## Chapter 3: THz Profilometry for Moisture Detection

### 3.1 Moisture in Art Conservation and Civil Engineering

Moisture and soluble salts are the main causes of degradation of mural paintings, in particular, frescoes. Water is the “driving force” of damage such as the detachment of the painted layer or the whitening of the painting due to the crystallization of salts (efflorescence). Indeed, the appearance of efflorescence is related to the alterations caused by moisture in the process of the evaporation of water through the surface of the wall. Early detection and location of the presence of moisture under the wall surface is therefore essential for avoiding such kind of damage. In particular, moisture content (MC) is known to be the main source of damage in frescoes for two main reasons. Because of the water diffusion and its eventual evaporation from the surface which can deteriorate or detach the fresco painting (direct effect) and the moisture diffusion through the plaster which causes the phenomenon of efflorescence, i.e. the whitewashing of the wall surface due to the crystallization of soluble salts such as nitrates and sulfates (indirect effect).

Therefore, an accurate diagnosis of the cause and the extent of the moisture is a fundamental step in the conservation of wall paintings. Such techniques are useful for periodically monitoring the conditions of a fresco in terms of a MC map of its surface, for early diagnostics, contributing to the detection of in-depth humidity and salts and for giving insight about the absorption dynamics of water (or water-based products) in the areas to be treated during the restoration phase.

Some of the currently used techniques by restorers are quite invasive such as gravimetric and chemical investigations. In these cases, a small sample of material from the painted surface has to be taken and be applied to standard chemical methodologies. Apart from the invasiveness of such a procedure, this approach only gives information about the surface characteristics, while the sub-superficial ones cannot be investigated without increasing the invasion of the measurement. Actually, in order to ascertain the deeper chemical composition of the painting substrate, a small hole (of the order of 1–2 mm diameter) needs to be drilled in the plaster. This kind of intervention cannot be performed everywhere on the painting; thus, the sample usually comes from regions away from the location in interest. Other non-destructive techniques are Evanescent Field Dielectrometry (EFD), Nuclear Magnetic Resonance Spectroscopy (NMR) and IR Thermography. These methods can mainly give qualitative analysis without giving a definition of the specific location of the moisture presence<sup>60, 61, 62</sup>.

Similar problems are observed in the field of civil engineering. When the water penetrates a concrete structure can cause cracks and also create a way for air to penetrate and attack reinforcing steel inside causing the steel to corrode. As a result,

the strength of the concrete structure decreases. To prevent this sort of deterioration, it is important to detect the diffused water and subsequently the induced cracks and defects, and repair them as early as possible. The most common technique used for this purpose is visual inspection when the concrete surface is exposed. However, the walls of buildings and tunnels are often covered with paints, wallpapers, or repairing materials, making visual inspection not possible.

To overcome the limitations of current technologies, THz imaging could be used as a novel technique. The detection of moisture is such a natural fit for THz imaging because of the highly absorption of water in the THz frequency range, while most materials which absorb moisture are either very transparent (eg. paper, plastics, cork, wood) or reasonably transparent to THz radiation as is going to be shown later in our results. Consequently, there a high contrast in the THz image between “moist” and “dry” regions can be achieved. The high permittivity of liquid water is typically the dominate contrast mechanism for moisture detecting by THz imaging.

Another property of THz imaging that fosters its use for moisture profilometry is its ability to resolve structures comparable in size to the electromagnetic wavelength of the THz radiation. Typical spatial resolutions for ~1 THz radiation are limited by diffraction effects to ~300  $\mu\text{m}$ , which enables one to image water diffusion into comparably sized cracks and voids in concrete and walls, which are quite porous media. While the presence of small cracks in materials may not create a large contrast in “dry” THz absorbance images, the penetration of a liquid with high permittivity into those cracks will produce an enhanced contrast in “wet” THz absorbance images.

Furthermore, THz radiation is not ionizing (photon energy at 1 THz ~4.1 meV) which is an important advantage making THz imaging non-harmful for operators. In addition, THz imaging is non-invasive, non-contact and one can obtain real time in situ measurements. Thus, a combination of THz profilometry with the already existing techniques could become a very powerful tool for both art conservators and civil engineers.

### **3.2 Demonstration of the THz-TDS reflection system**

In this section will be demonstrated how our homemade THz-TDS reflection system in combination with our imaging program, operates. For this purpose a sample consisting of a first layer of aquarelle paper, which covers a second layer with a chess-like pattern, made of aquarelle paper and aluminum foil (Figure 27 (a)), was prepared. An area of 21 x 12 mm was scanned in the X-Y plane with a step size of 1 mm, which is close to the THz beam spot size at focus, which is around 800  $\mu\text{m}$ .

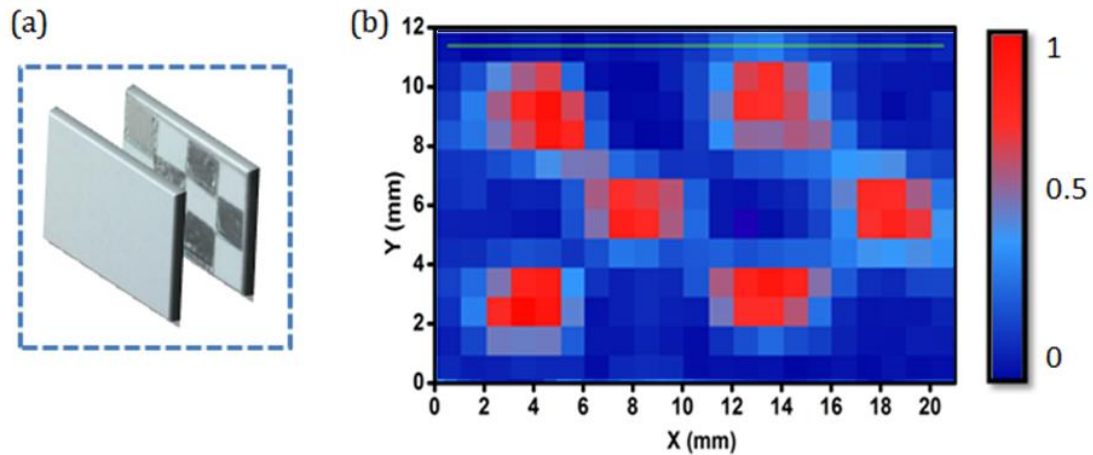


Figure 26: (a) Stratified sample consisting of aquarella paper and aluminum foil. (b) Reconstructed image (using Labview).

The THz electric field was recorded for every point of the sample. From the areas with alluminum foil, only two reflection peaks were expected. One from the first surface -aquarelle paper- and the other one from the aluminum foil which is opaque for THz so it totally reflects the THz radiation. On the other hand, a spot without aluminum foil gives a THz electric field with three reflection peaks, from the two aquarelle papers and from the metallic surface which is used as the sample holder. Both cases are presented in Figure 28.

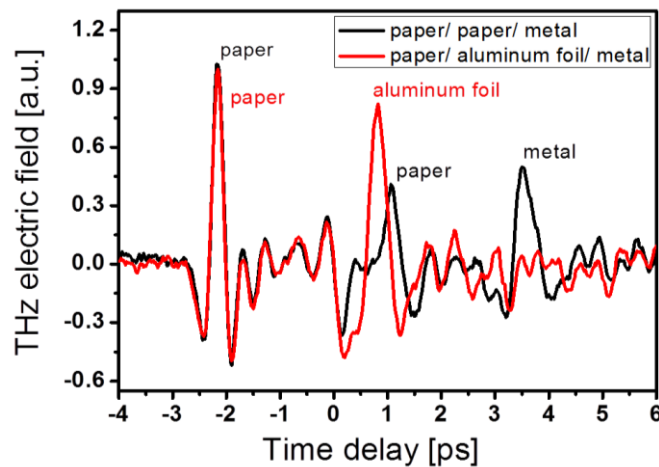


Figure 27: THz electric fields of two different spots with and without aluminum foil.

Using the analysis described in section 2.4.2, the image of the sample was reconstructed, as is illustrated in Figure 27 (b), where the red color means higher reflection signal whereas blue means lower. This result demonstrates the ability to obtain images of hidden objects as long as the used material is at least partially transparent to THz radiation.

### 3.3 Selection of proper sample material

Having tested the proper functioning of our system, a search for the most suitable material to be used as host medium for our samples was held. A suitable material should have some of the following properties. First, it should be totally or partially transparent to THz radiation so an indepth analysis could be possible. Secondly, it should have a relatively large reflection signal so the system can detect it. This depends mainly on two parameters; the optical properties of the material such as refractive index and absorption coefficient and the surface on which THz beam hits the sample, should be as smooth as possible. This happens because in case of materials with a rough surface, diffuse scattering reduces the power reflected in the specular direction. Furthermore, the material should be water absorptive and commonly found on walls.

Our samples are placed on a metallic surface of our holder and then pressed onto it with a plastic frame so they remain stable, as is shown in Figure 29. The sample holder is then placed on the XYZ translation stage of our system.

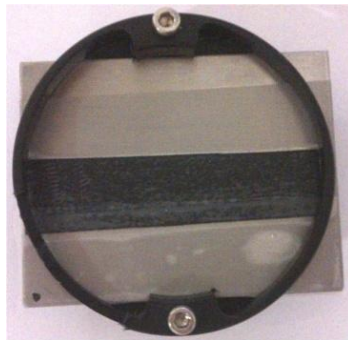


**Figure 28: Paper sample on the sample holder.**

Different kind of materials that had already been studied in the literature, were tested. Some of these materials are wood<sup>63-66</sup>, cork<sup>67-69</sup>, polymers<sup>70-73</sup>, cotton<sup>74</sup>, paper<sup>39,66,75,76</sup>, cement<sup>41,42,77</sup> and gypsum<sup>41,78,79</sup>. In Figure 30 are shown the measurements of these materials in our THz-TDS reflection setup with a 500  $\mu\text{m}$  thick crystal in the detection. The main criterion for choosing the “right” material is its transparency to THz radiation as has already been mentioned. This means that in the electric fields of Figure 30, two reflection peaks must be present, first one from the surface of the material and second one from the metal surface of the holder. Thus the selected materials are the two different kinds of paper and gypsum. Gypsum, except its good properties, is also a material used in real buildings, walls and mural paintings. Paper samples were used for some initial measurements due to the fact that are easier to be handled. Also, due to their transparency to THz radiation, were ideal candidates for the manufacturing of stratified samples with discrete surfaces.

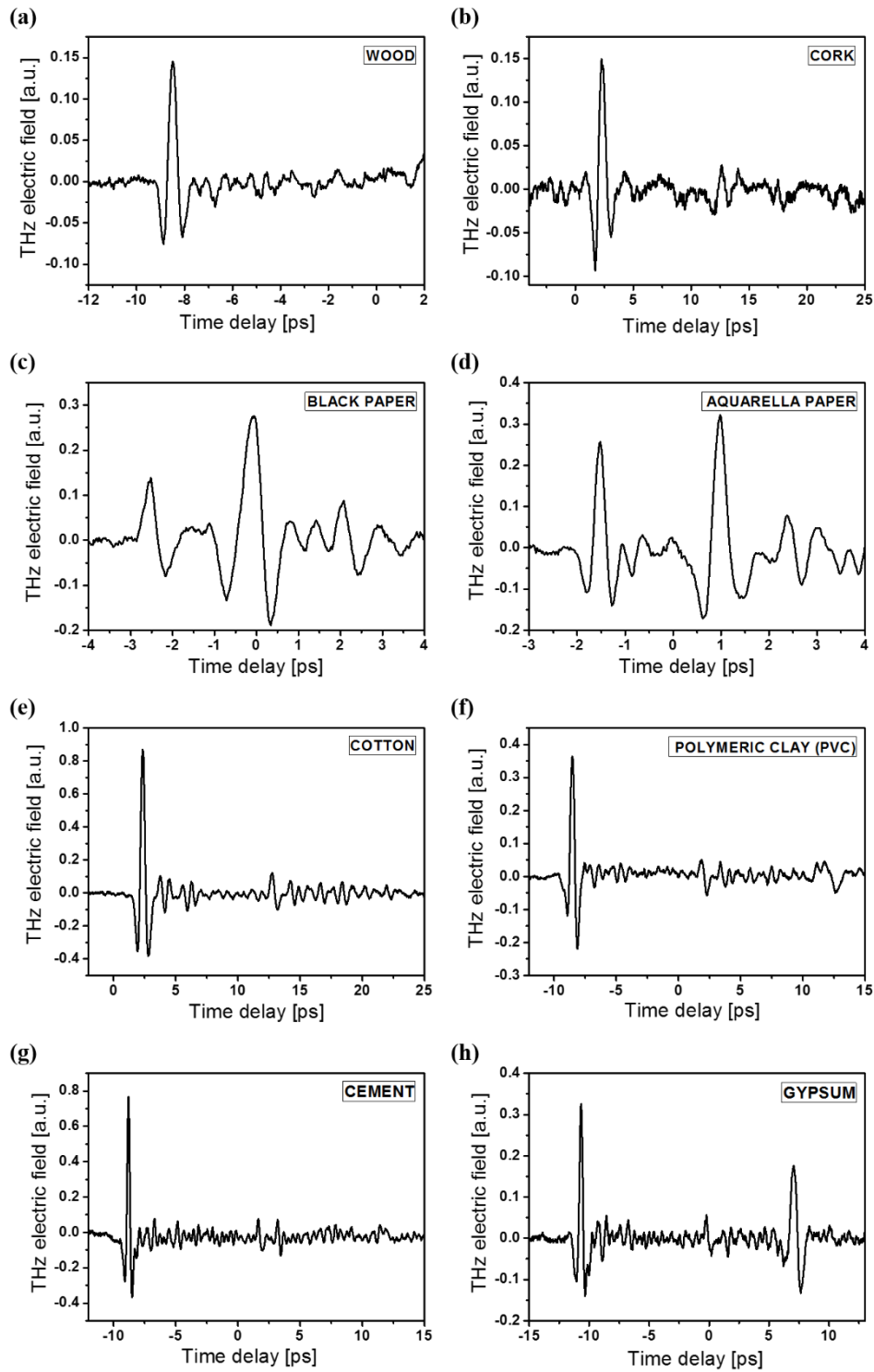


**Figure 29: Reflection THz electric fields for several materials (500  $\mu\text{m}$  ZnTe detection crystal).**

Subsequently, the selected materials were optically characterized (see Figure 31) in the THz frequency regime using the analytical equations described in section 2.4.1. Looking at the absorption coefficients one can see that there isn't any absorption peak in any particular frequency. We also extracted their refractive indices which are quite stable for these frequencies. In particular, the refractive indices for black paper, aquarella paper and gypsum are 1.09, 1.56 and 1.64 respectively. These

measurements were performed in our THz-TDS transmission setup. For the paper samples (black paper and aquarella paper), an 1 mm thick ZnTe crystal was used in the electro-optic detection whereas while for the gypsum samples, was used a 100  $\mu\text{m}$  thick GaP crystal. Our results are similar to the litterature.

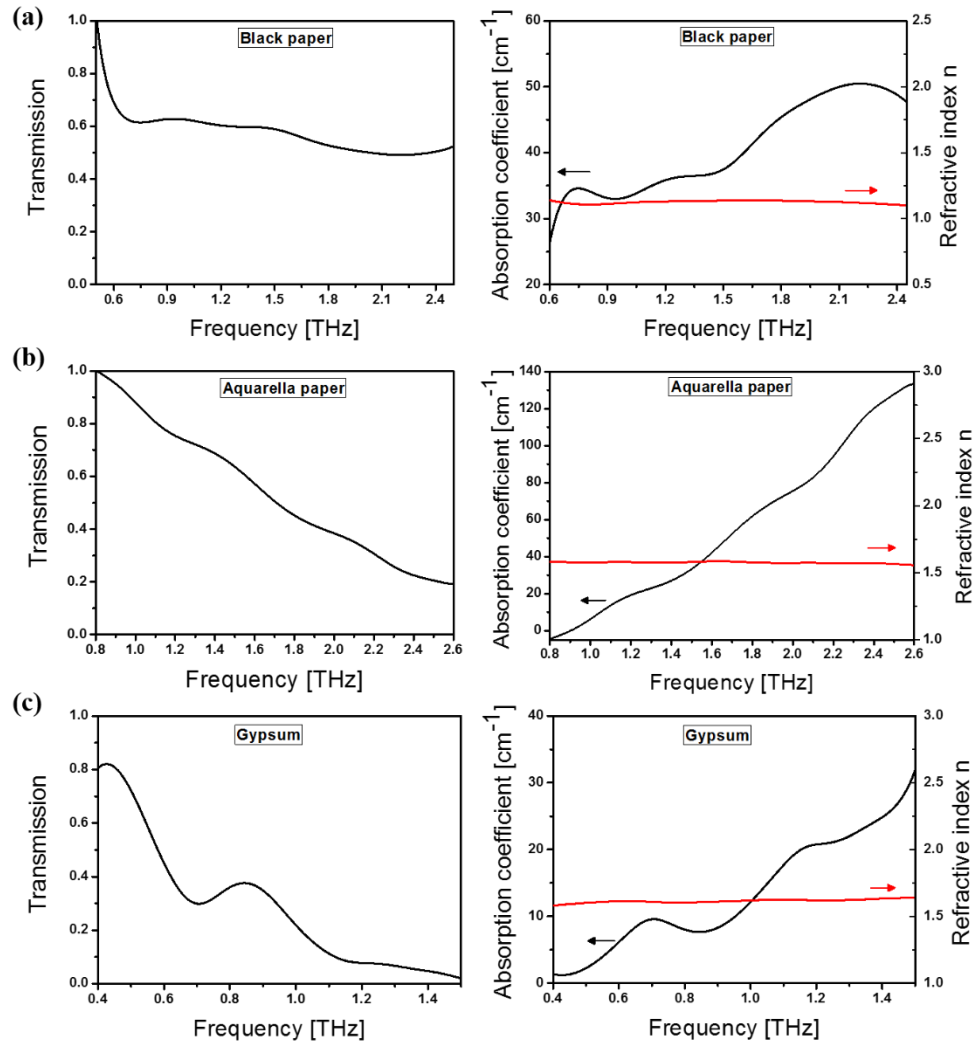


**Figure 30: Transmission, absorption coefficient and refractive index of (a) a 0.28 mm thick black paper, (b) a 0.24 mm thick aquarella paper and (c) a 2.41 mm thick piece of gypsum. (a) and (b) were measured with 1mm thick ZnTe detection crystal and (c) with a 100 $\mu\text{m}$  thick GaP detection crystal.**

### 3.4 Moisture detection on paper samples

#### 3.4.1 Sample preparation

In this part of the experiments, samples of different and known moisture contents (MC) were prepared. Moisture content express the amount of water present

in a moist sample and can be expressed on wet or dry basis. In our case the dry basis scenario was chosen and is described by the formula below:

$$MC = \frac{m_{wet} - m_{dry}}{m_{dry}} \times 100\% \quad (3.1)$$

where  $m_{dry}$  being the sample's weight after drying on a hot plate for a few minutes and  $m_{wet}$  the sample's weight after immersion in a bath of water and drying on air for different periods of time depending on the desirable MC. Following this procedure, moisture was distributed as homogeneously as possible in the entire sample's volume.

After placing the samples in the holder, plastic wrap was used to cover the samples and prevent water evaporation and subsequently change of the MC, during measurements.

### 3.4.2 Surface detection and Imaging

First we wanted to investigate if it was possible to distinguish wet samples from dry ones and also wet with different moisture contents with our THz-TDS system. For this purpose paper samples of two different types, black paper and aquarella paper, were used.

#### Black Paper

A description of the samples is displayed in Table 2 and Figure 33 (a) shows how they were placed on the sample holder. Sample A is consisted of a fully wet paper and a dry one which are separated by a metallic area of the sample holder. The same geometry is employed for all samples in this section. In Sample B, the first paper has MC=7.9% and the second MC=26% while in sample C the first paper has MC=4.7% and the second one has MC=46%. Sample D has a paper with MC=4.4% and another one with MC= 56.5% and sample E has a paper with MC=5.8% and one with MC= 11.3%. The scanned area was slightly different for every sample, 4 x 16 mm for sample A, 3 x 9 mm for B, 3 x 12 mm for C and D and 3 x 10 mm for sample E with the step size to be 1 mm.

	Upper paper (MC)	Metal	Lower paper (MC)
<b>Sample A</b>	Fully wet	— —	Dry
<b>Sample B</b>	7.9%	— —	26%
<b>Sample C</b>	4.7%	— —	46%
<b>Sample D</b>	4.4%	— —	56.5%

<b>Sample E</b>	5.8%	-  -	11.3%
-----------------	------	------	-------

**Table 2: Moisture content combinations of the samples.**

In Figure 32, THz electric fields of one spot in the different regions of every sample are shown. The main difference between wet and dry paper is the fact that for the dry one, two reflection peaks are obtained (from the paper and the metal) whereas for wet paper, regardless of the moisture content, the peak from the metallic surface disappears. This occurs because THz waves are strongly absorbed by water molecules, making paper -a material relatively transparent to THz radiation- opaque. This fact is exploited to extract the images of sample A (Figure 33 (b)).

In the images, an interpolation of the pixels has been applied in order to smooth them. With heavy blue area is represented the wet part, with light blue the dry paper and with red the metallic surface. From the images it is obvious that we are able to distinguish a wet from a dry sample.

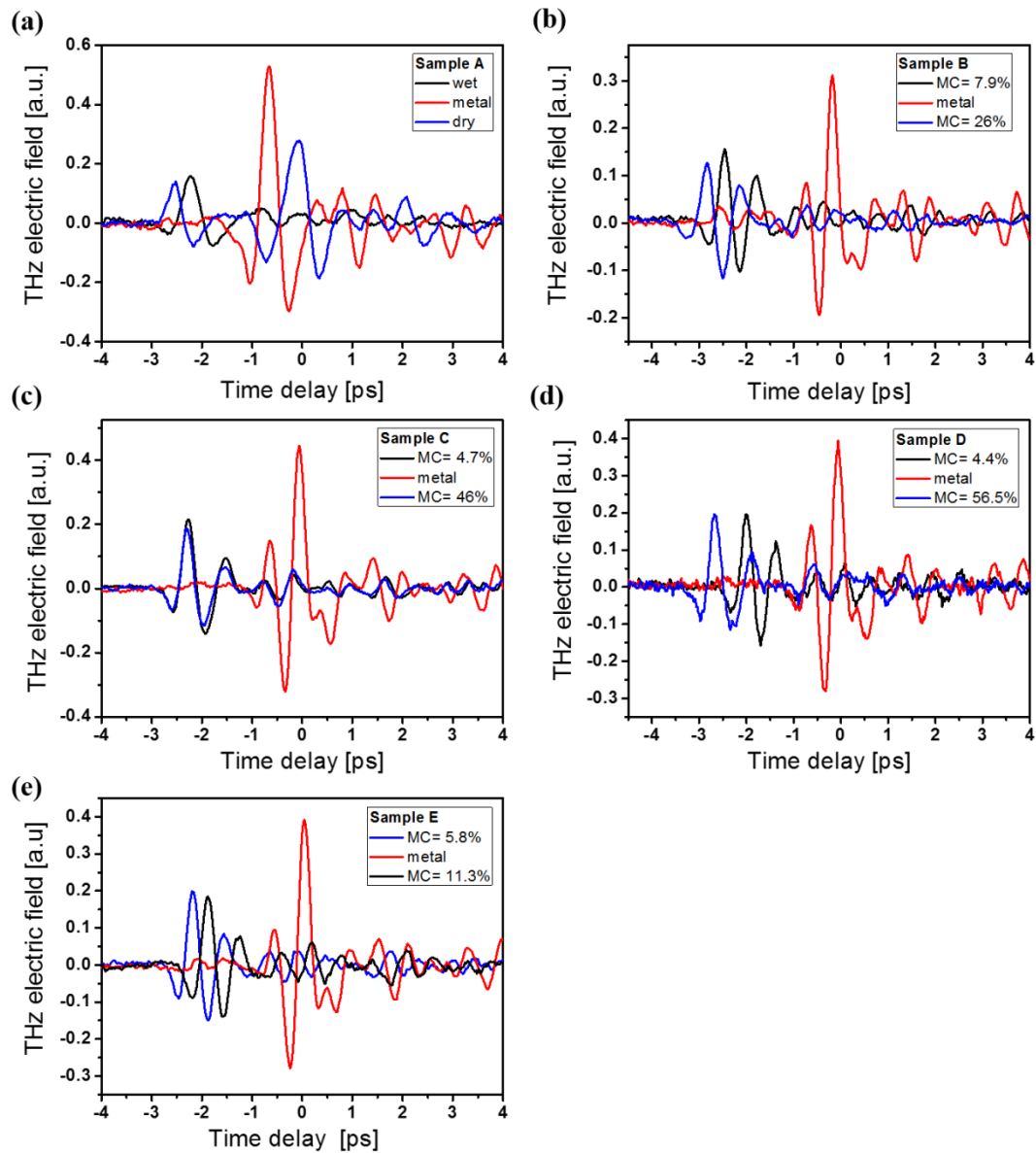


**Figure 31: Reflected THz electric fields of the samples of table 1.**

A step further was to investigate the possibility to distinguish different moisture contents (Table 2-samples B, C, D, E). The only information in this case is the first peak which is more or less the same between the samples apart from some minor changes in its amplitude that can not be taken into account. Also, small differences in the position of the peaks may occur due to differences of the sample's thickness or the way that is placed onto the holder. The reconstructed images are very similar between samples B to E (Figure 32 (b)), which means that it was not possible to distinguish papers with different MC between one another.

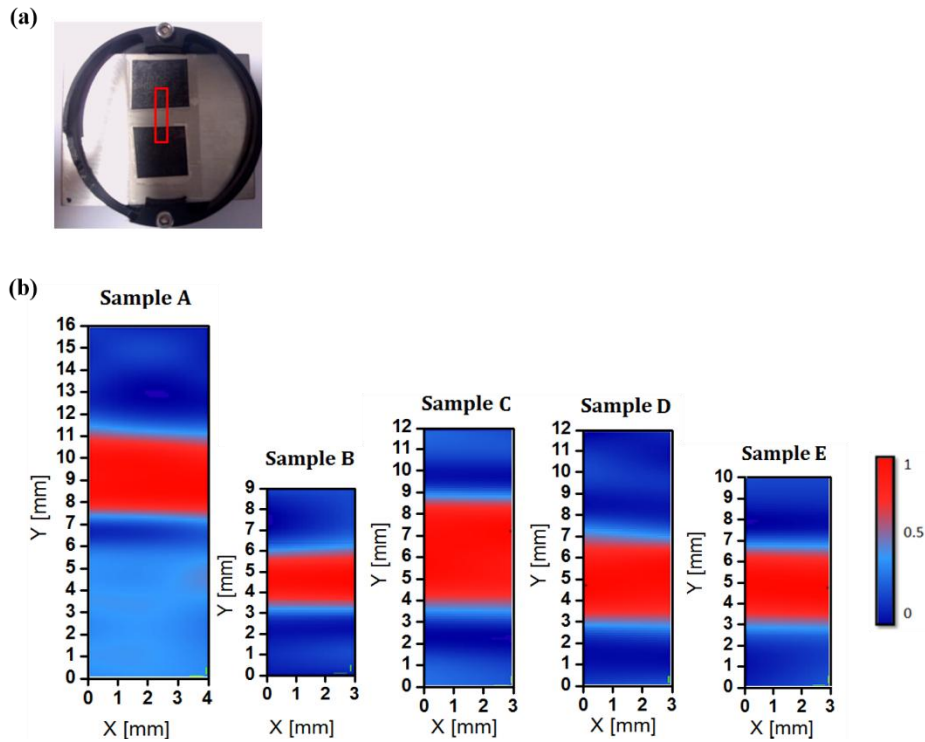


Figure 32: (a) Sample holder. The red rectangular shows the area of the sample that was scanned. (b) Reflection images of the different samples A, B, C, D, E.

### Aquarella paper

For aquarella paper, transmission measurements were performed (Figure 33 (a)) for samples with different moisture contents (MC=0% -100%). A calibration curve (Figure 33 (b)) was constructed in order to see if it is possible to distinguish different moisture contents. The samples used, were a piece of paper dried on a hot plate (Sample A). Sample B is in ambient air, Sample C has MC= 20%, sample D has MC= 40%, sample E has MC= 60%, sample F has MC= 80% and sample E has MC=100%.

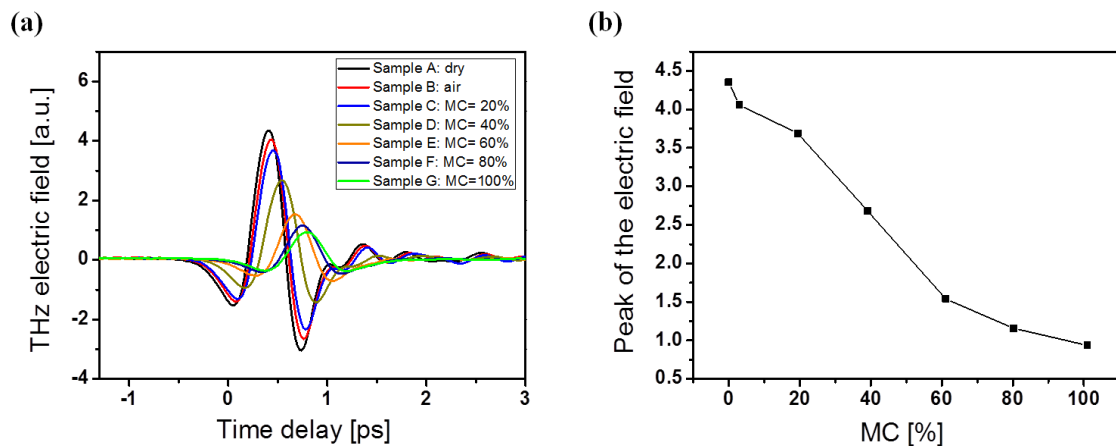


Figure 33: (a) Transmission THz electric field of aquarella paper with different MC. (b) Calibration curve of MC in relation to THz field's intensity.

From the THz electric fields in Figure 33 (a), one can observe that as the moisture content increases, the peak intensity decreases, the pulse broadens and a displacement of its initial position in time is observed. These can be explained by the fact that when water is added, the absorption coefficient of the sample increases as well as its thickness. In Figure 33 (b) is obvious that different moisture contents can be distinguished.

With the calibration curve we have shown that it is possible to distinguish different moisture contents with our transmission system. Using the samples of Table 3 we are going to investigate if we can do the same with measurements in our reflection setup. Figure 35 (a) shows the samples placed on the metallic surface of the sample holder. The scanned area to be imaged was 3 x 7 mm for sample A, 2 x 79 mm for B, 2 x 11 mm for C with 1 mm step size.

	<b>Upper paper (MC)</b>	<b>Metal</b>	<b>Lower paper (MC)</b>
<b>Sample A</b>	Dry	- -	53%
<b>Sample B</b>	6.5%	- -	50.6%
<b>Sample C</b>	15.6%	- -	50%

**Table 3: Moisture content combinations of the samples.**

The corresponding electric fields are shown in Figure 34. The signal is less noisy and unlike black paper, in the samples with low moisture content, both reflection peaks appear in the electric fields. This means that aquarella paper is less water-absorbent material. One can, also, see that the first peak in all cases is higher when moisture content is larger. This is because the reflected amount from an interface increases as the difference of the refractive indices increases.

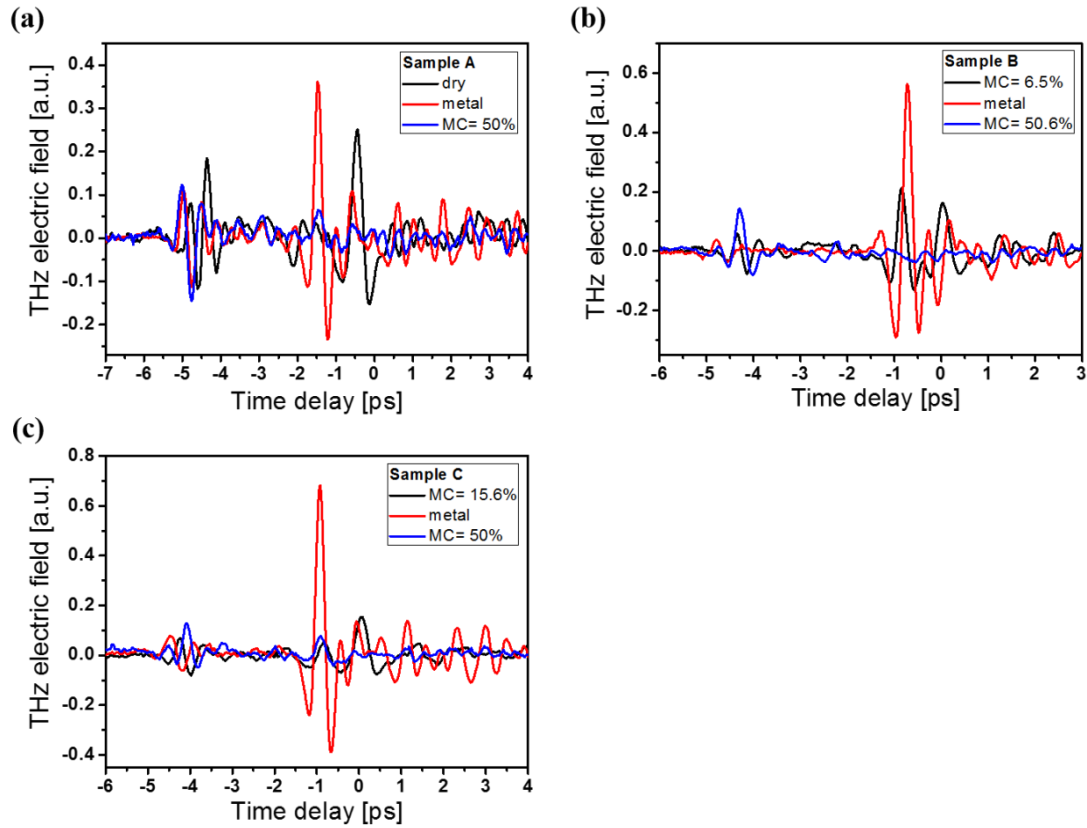
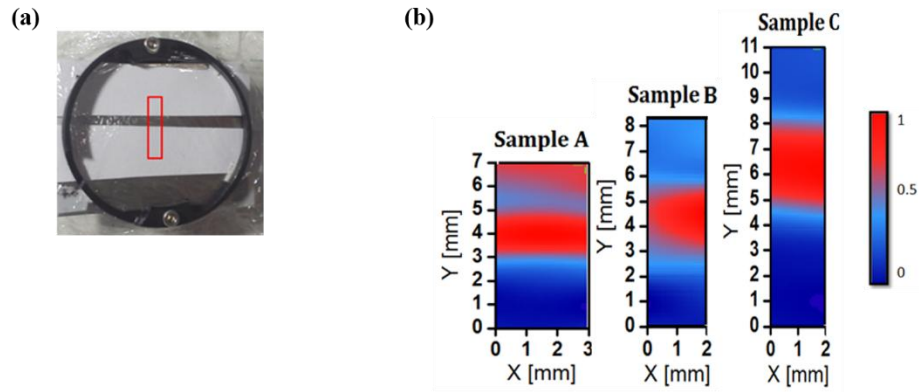


Figure 34: Reflection THz electric fields for samples of table 2.

In the reconstructed images of Figure 35 (b) the difference between the dry and the wet paper (Sample A), is obvious and more clear than in the previous case of the black paper. This implies that aquarella paper is more transparent to THz radiation than the black one. An other interesting aspect is that the difference in moisture content of the papers with  $MC_{\text{sample C}}=15.6\%$  ,  $MC_{\text{sample B}}=6.5\%$  from sample A and B, is also visualized. This is an indication that different moisture contents can be identified. However, when samples with smaller moisture content differences were tested, the images were similar to each other as in the case of black papers. Also, it was not possible to retrieve the value of an unknown moisture content neither from the image nor from the electric field.



**Figure 35: (a)Sample holder. The red rectangular shows the area of the sample that was scanned (b)Reflection images of the different samples.**

As a conclusion of this section, the possibility of distinguishing wet from dry paper samples and also wet samples with large differences in their moisture contents, was demonstrated through a qualitative analysis. This type of information could be useful for the optimisation of the paper fabrication process where the drying process is a very important part as it has a strong impact on the final paper quality. The movement and distribution of the moisture during the drying process influences paper properties such as shrinkage, curl, strength, etc. Non-uniform moisture profiles can lead to various problems such as an increased fracture probability, difficulties upon reel formation, calendar blackening, printer misfeeding, and curling and cockling of paper. Online monitoring of the moisture content is hence an important task during the drying process.

### 3.3.3 In depth detection and Imaging

In this section, an in depth moisture investigation is discussed. For this purpose, aquarella papers were attached together to create a stratified sample. Between dry papers, wet ones were introduced and between every layer, plastic wrap was placed, to prevent water penetration from wet to dry papers. The thickness of a single paper is  $\sim 0.24$  mm and the thickest sample was around 1 mm. In Figures 36-38 are shown the different samples with varying number of layers and the corresponding reflected THz electric fields.

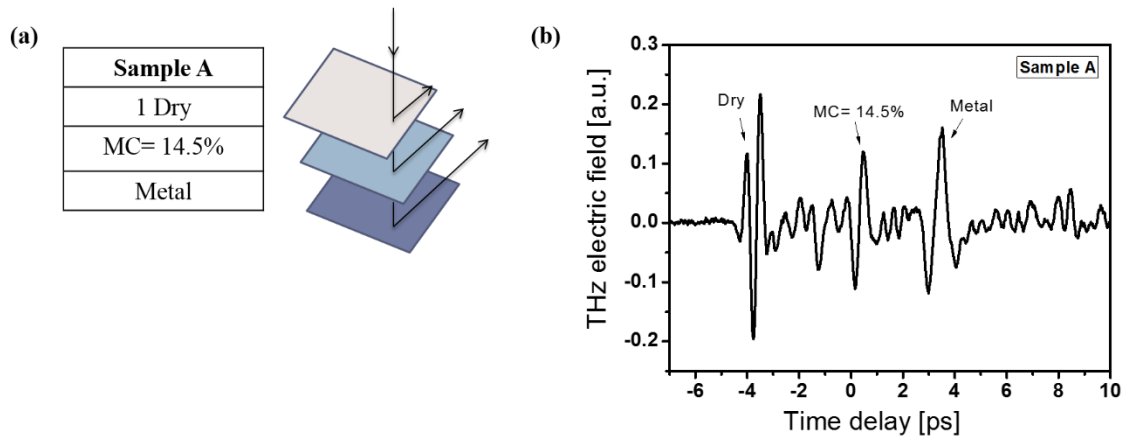


Figure 36: Stratified sample A and the corresponding reflected THz electric field.

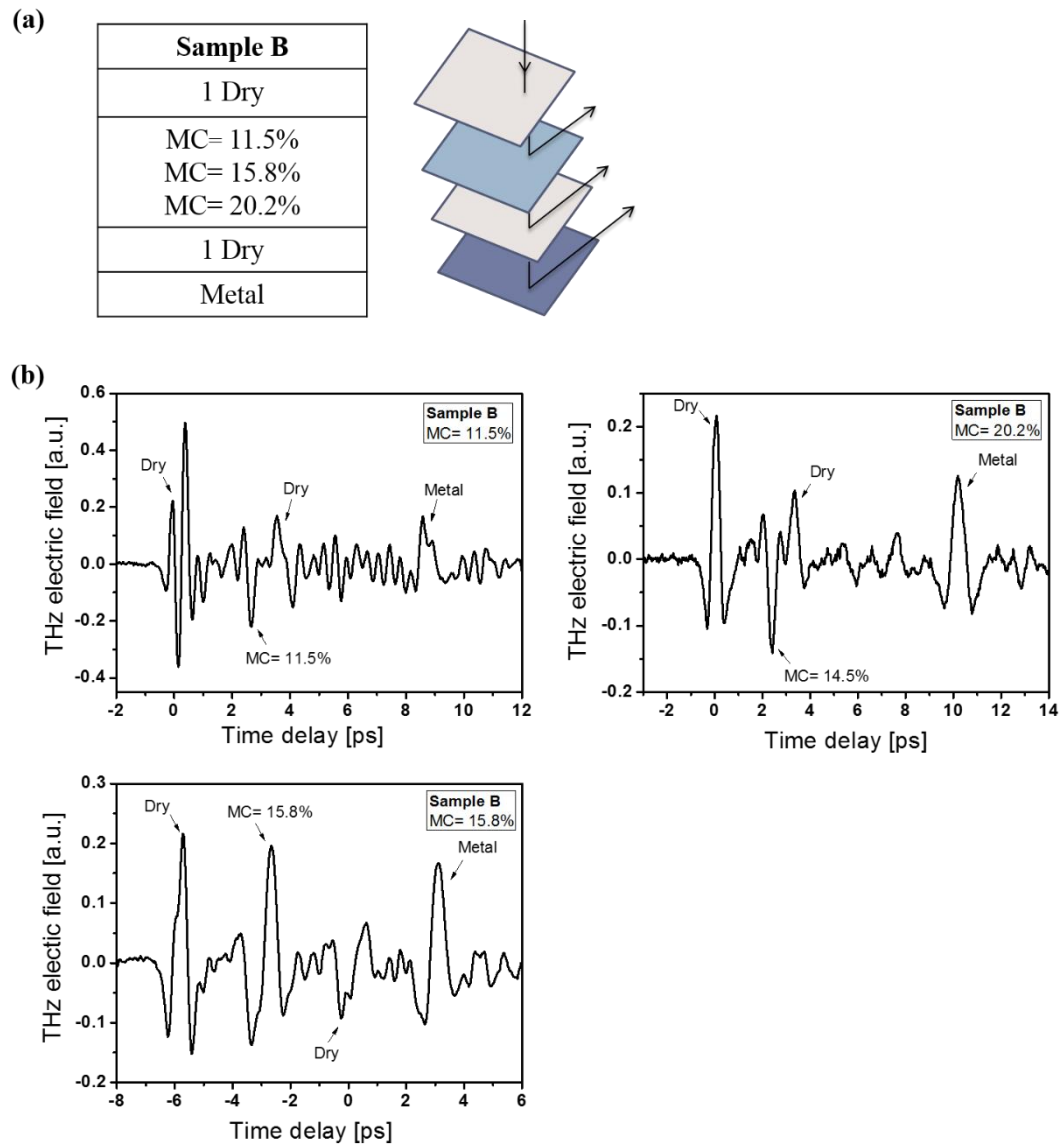


Figure 37: Stratified sample B and the corresponding reflected THz electric field.

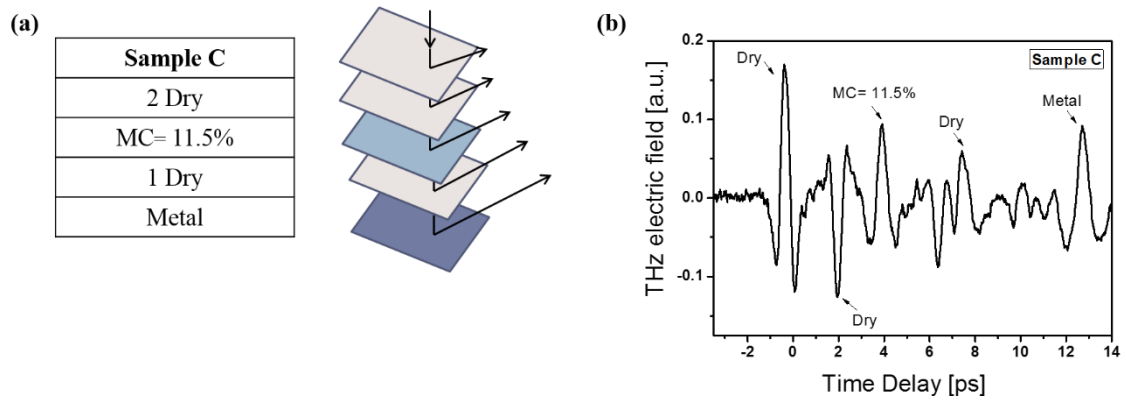


Figure 38: Stratified sample C and the corresponding reflected THz electric field.

In Figure 36, the more simple case is shown where a dry paper covers a wet one. From the corresponding electric field one can see that there is a reflection peak from every layer, including the wet paper which means that is detectable. In Figure 37 an extra dry paper is introduced under the wet one. In this case three different moisture contents were tested and in all the corresponding electric fields one can see the peak of the wet samples. The same conclusions can be extracted from Figure 38 where one more dry paper was added on top of our sample. Again we have a clear echoe from the wet surface.

An other group of samples was prepared, where a half wet /half dry paper was placed under two and three paper layers respectively, as shown in Figures 39,40.

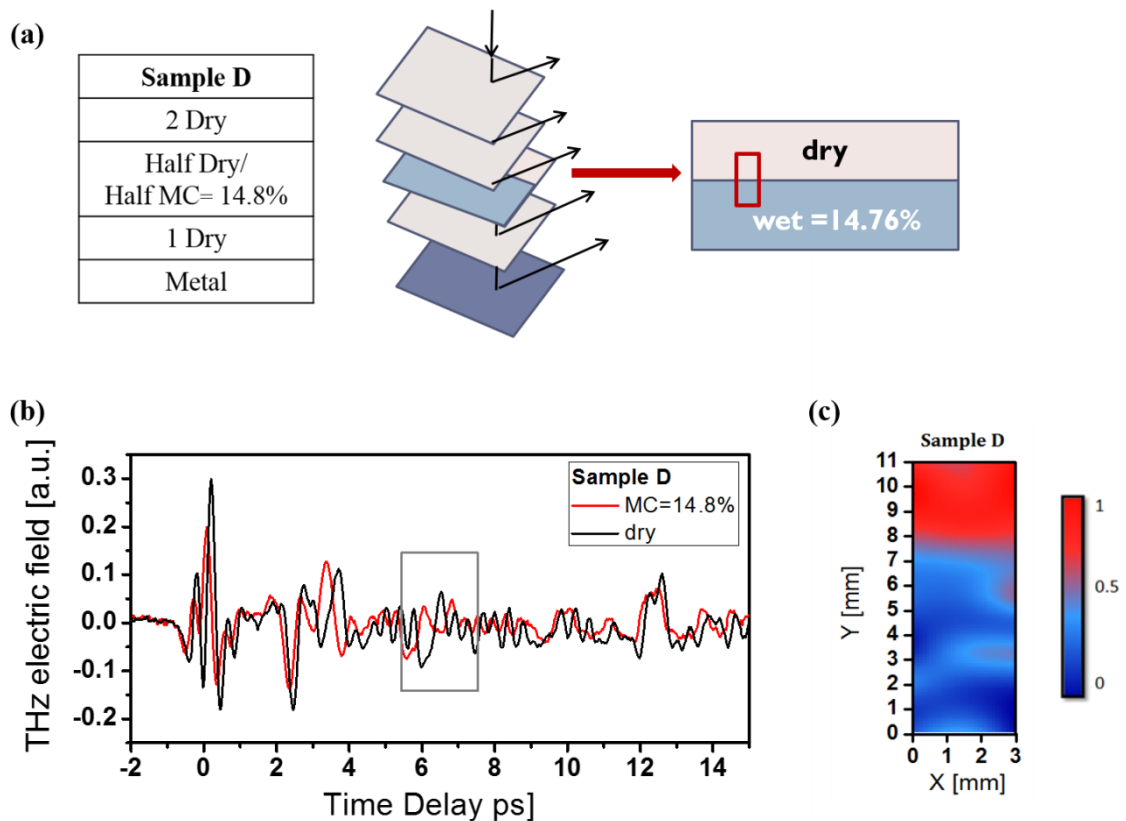


Figure 39: (a) Sample D: A stratified sample composed of two layers of dry aquarella paper, a half dry - half wet (MC=14.8%) paper layer, one more dry paper layer and a metallic surface. (b) Reflection THz electric

field from two spots, one in the dry area and one in the wet. (c) THz image of the third layer showing the dry (red) and wet (blue) region.

The corresponding images along with the electric fields of two different spots in wet and dry area, are illustrated in Figure 39 and Figure 40. In the electric fields, one can see the reflection peaks of every separate layer like in the previous samples. The main difference between the two regions, is that for the wet region there is a decrease in the intensity, of the peaks from the semiwet paper and the metal. This is because water absorbed part of the radiation. This fact is exploited for the reconstruction of the images, where the difference between dry (red) and wet (blue) region on the sample is clearly shown.

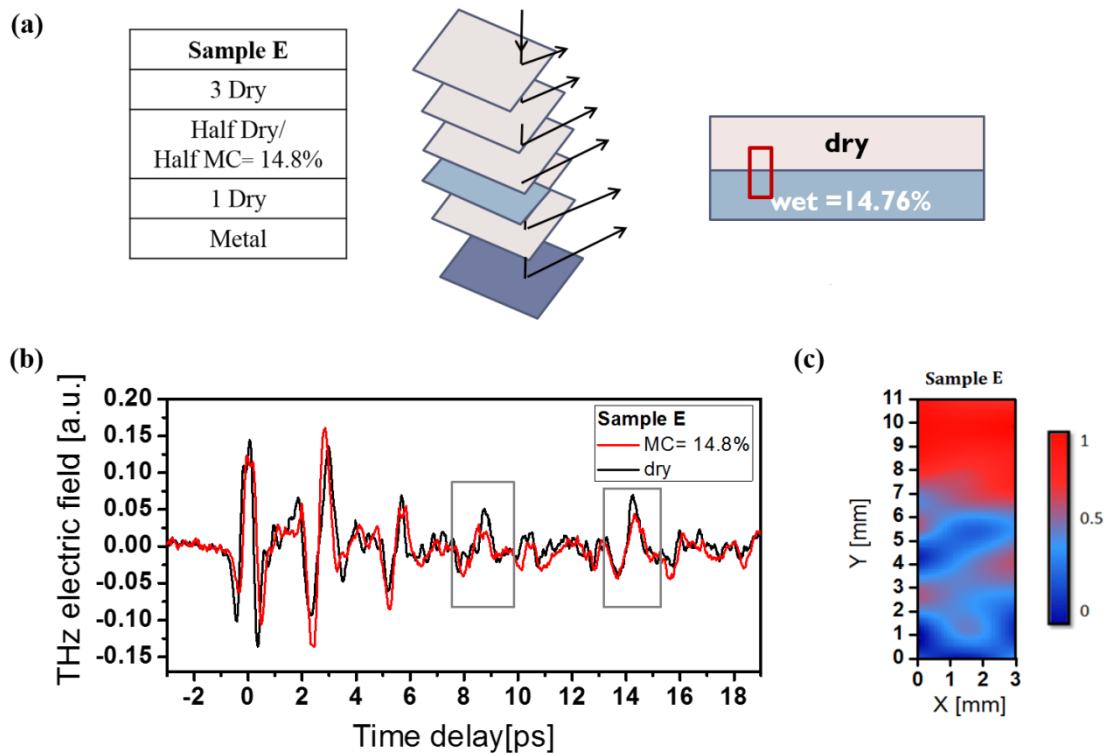


Figure 40: (a)Sample E: A stratified sample composed of three layers of dry aquarella paper, a half dry - half wet (MC=14.8%) paper layer, one more dry paper layer and a metallic surface. (b) Reflection THz electric field from two spots, one in the dry area and one in the wet. (c) THz image of the third layer showing the dry (red) and wet (blue) region.

Summarizing, in this section the ability to detect in depth ( $d \sim 0.75$  mm) moisture was demonstrated and through reconstructed THz images it was possible to distinguish wet from dry regions of our stratified paper samples.

### 3.4 Moisture detection on gypsum samples

In previous sections, the ability of our system to detect surface and in depth moisture, was demonstrated for paper samples. The next step is to use a more realistic material as sample and using the same principles as before, detect and give an approximation of the location of the moisture front. The ultimate goal is to detect the interface between wet and dry sample which is created due to the difference of refractive indices which for dry gypsum is  $n_g=1.6$  and for water is  $n_w=2$ . The challenge in this situation is the fact that the change of the refractive index between dry and wet sample is going to be smooth with no sharp boundary due to the nature of our material. Also the difference of refractive indices  $\Delta n=0.4$ , is relatively small, thus, difficult to be detected.

#### 3.4.1 Sample preparation

The gypsum samples were made out of two parts of plaster-of-paris (calcium carbonate/calcium sulfate semihydrate/silica), which is in powder form, and  $2^{1/2}$  parts of water. This mixture was then placed in molds and dried in air for a day. The thicknesses of our samples are between 0.8 mm and 1.8 mm. The thickness is measured with a micrometer. A syringe was used to wet (a few droplets) the samples and in some measurements plastic wrap was placed between samples to prevent water penetration from one to the other. The samples are placed on the metallic holder as in the case of paper samples. All measurements were made with an 1 mm ZnTe crystal in the electro-optic detection. Also, for every measurement, the noise has been removed, for clear and less noisy results. This means that after every measurement, the noise was recorded (THz beam is blocked and the IR is only recorded), and then was subtracted from the corresponding THz electric fields.

#### 3.4.2 Indepth moisture detection

First, we need to see how our samples behave when water is added. Figure 41 shows the electric fields of a 1.83 mm thick gypsum slab while it is dry, after adding water and when a few minutes (~10 min) have passed and water has been fully absorbed. For the dry gypsum sample two peaks are present, first from air-gypsum interface ( $t_1=-10.4$  ps) and the second one from gypsum-metal interface ( $t_2=7.2$  ps). When water is added the intensity of the first peak increases while the second one disappears. This is due to the increase of sample's refractive index and absorption coefficient. Thus, the first peak's intensity rises because larger  $\Delta n$  corresponds to bigger amount of the reflected THz radiation and the second peak disappears because THz radiation is absorbed by the added water.

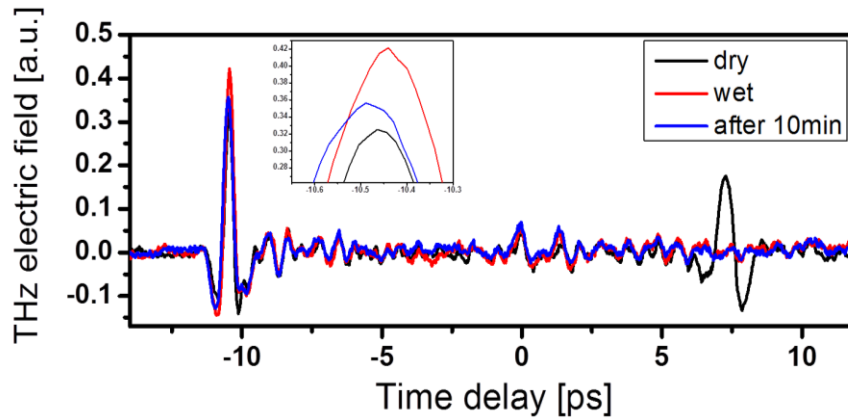


Figure 41: Reflected THz electric field of dry and wet gypsum. The inset shows the intensity increase of the first peak when water is added.

During the measurements it was realized that for our sample thicknesses it is very difficult to create an interface because the water penetration in gypsum happens very fast. The idea was then to use two different pieces of gypsum, attach them together, and create an artificial interface. Figure 42 shows the different samples that we used and the corresponding THz fields before the addition of water.

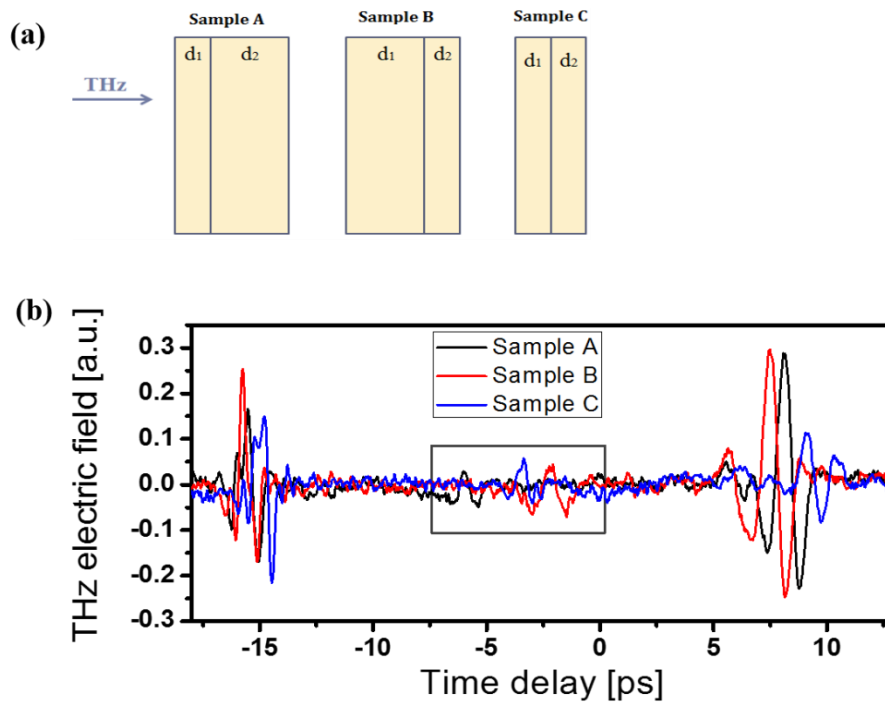
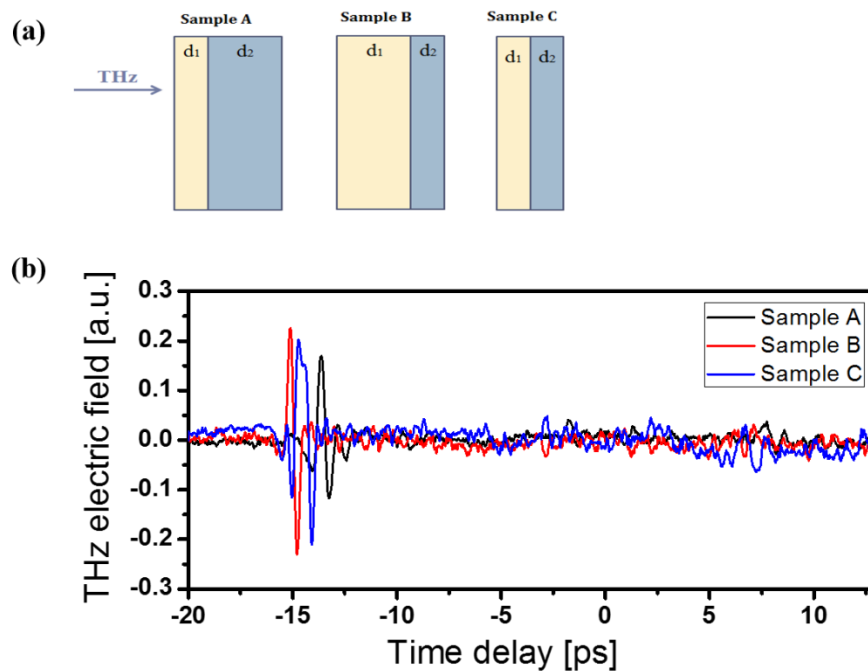


Figure 42: (a) Sample A is composed of two gypsum pieces with  $d_1=1.08$  mm and  $d_2=1.48$  mm, for sample B is  $d_1=1.48$  mm and  $d_2=1.08$  mm and for sample C  $d_1=0.90$  and  $d_2=1.05$  mm. (b) Reflected THz electric fields and corresponding spectra (c).

In all three cases the electric field has three peaks, the first one from the air-gypsum interface and the third one from the gypsum-metal interface. Both peaks are located around the same position with small deviations due to differences in the thickness of the samples. The second peak for all three samples (see the square on Figure 42) comes from the interface between the two gypsum pieces. The position of the second

peak depends on the thickness of the first gypsum piece. To ensure that these peaks come from the gypsum-gypsum interface, we calculated the thickness of the samples as it was demonstrated in section 2.4.2. For sample A:  $\Delta t_1=0.99$  ps  $\rightarrow$   $d_1=0.89$  mm and  $\Delta t_2=1.42$  ps  $\rightarrow$   $d_2=1.3$  mm, sample B:  $\Delta t_1=1.22$  ps  $\rightarrow$   $d_1=1.37$  mm and  $\Delta t_2=0.98$  ps  $\rightarrow$   $d_2=0.87$  mm and for sample C:  $\Delta t_1=1.19$  ps  $\rightarrow$   $d_1=1.06$  mm and  $\Delta t_2=1.25$  ps  $\rightarrow$   $d_2=1.11$  mm. The calculations were made for  $n_{\text{air}}=1$  and  $n_{\text{gypsum}}=1.6$ . The calculated thicknesses differ from the ones measured by the micrometer due to inhomogeneities of the samples.

The same samples were then measured after water was added to the second gypsum piece (with the thickness  $d_2$ ), while the first gypsum piece (with the thickness  $d_1$ ) was dry (see Figure 43).



**Figure 43:** (a) Schematic representation of the samples. (b) Reflected THz electric fields.

In this case the second and third peaks disappear because the water diffuses from the wet to dry sample very fast so the dry piece becomes immediately wet, thus, THz radiation is absorbed in the water.

To slow down the water diffusion into our dry gypsum pieces, we placed plastic wrap between the two gypsum pieces. The water does not penetrate through the plastic wrap and a discrete interface is created. To see if the tape affects our measurements, we measure a dry sample, with and without the plastic wrap. From Figure 44 one can see that the plastic wrap is transparent to THz radiation (no significant change for the third peak from metallic surface) and the only difference is the higher second peak.

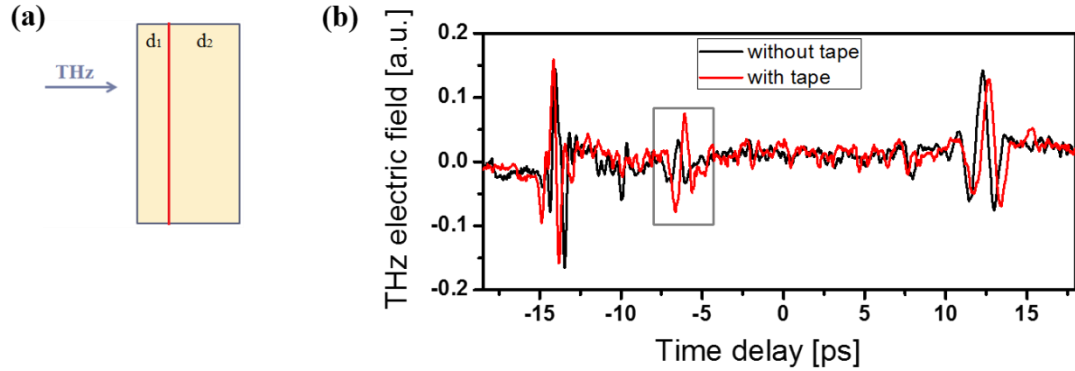


Figure 44: (a) Schematic representation of the sample with  $d_1=0.80$  mm and  $d_2=1.48$  mm. The red line represents the scotch tape. (b) Reflection THz electric fields of the sample with and without scotch tape.

After we tested the effect of the plastic wrap on the sample, next step is to add water to the second gypsum piece (with  $d_2$  thickness) and measure with and without the wrap. The results are shown in Figure 45.

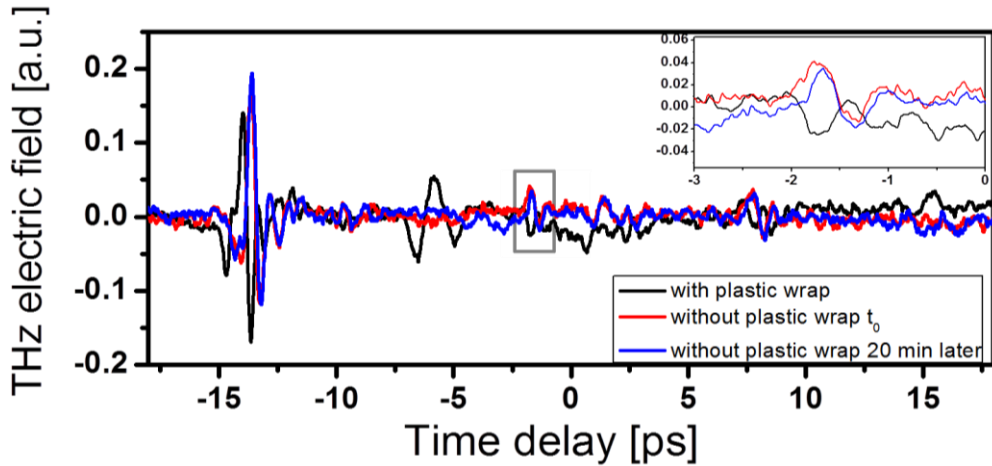
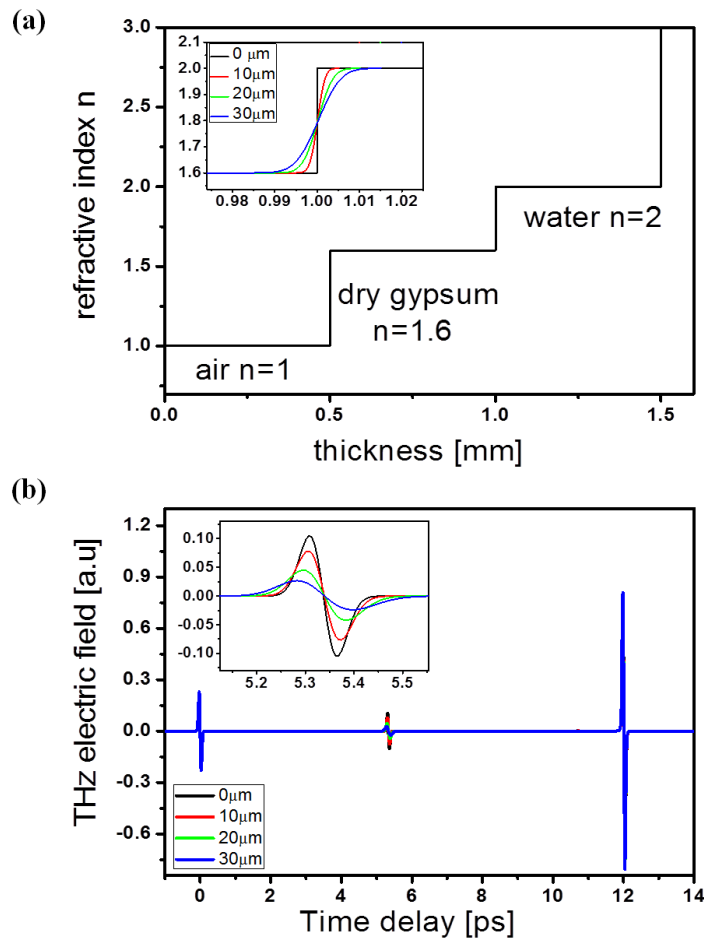


Figure 45: Reflected THz electric fields.

In this case, when the plastic wrap is present, the second peak ( $t_2=-5.84$  ps) is still present at around the same position as in the case of the dry sample. However, the third peak (the one that corresponds to the metallic surface) has disappeared because of the presence of water in the second gypsum piece.

We then remove the plastic wrap. The second peak has now lower intensity and its position has shifted ( $t_2=-1.78$  ps). Also for the same measurement after 20 minutes one can see that the peak is in the same position and there is a decrease in its amplitude. To explain this behaviour we numerically simulated THz field reflected from the model system which represents our samples. We considered a system which is composed of three regions with different refractive indices. First we have air ( $n=1$ ), second we have dry gypsum ( $n=1.6$ ), third we have water ( $n=2$ ) and the last part has infinite refractive index and it corresponds to the metallic surface of our sample holder. To simulate the diffusion of the water between the wet and dry pieces between

the layer with  $n=1.6$  and  $n=2$ , we introduced the transition layer where the refractive index changes smoothly from 1.6 to 2 by the error function law (see Figure 46 (a)). We considered four different situations, one with sharp boundary between dry gypsum and water, one with a transition layer of  $10\ \mu\text{m}$ , one with  $20\ \mu\text{m}$  and one with  $30\ \mu\text{m}$ . The increase of the transition layer thickness corresponds to higher penetration of the water into the dry gypsum piece. The reflected electric fields are shown in Figure 46 (b). The first peak comes from the air- gypsum interface, the second one from the gypsum-water interface and the third from the water-metal interface. One can see that while the transition width increases two things happen to our reflection peak. First, its amplitude decreases and second, it remains at the same position ( $t_2=5.3\ \text{ps}$ ).



**Figure 46:** (a) The system with the different refractive indices. The inset shows the four different widths of the transition layer. (b) The corresponding reflected electric fields.

Looking at our experimental data now, a possible interpretation of our results is that the shift of the second peak is due to the removal of the plastic wrap which thickness is around  $30\ \mu\text{m}$  and due to a slight misalignment of the sample as we removed it and then replaced it on the holder. The interesting thing though, is that for the two measurements taken after the wrap was removed, after twenty minutes the peak remains in the same position with a slightly decreased intensity which means that now we have a wider transition layer. This is an indication that the water has

penetrated more into the dry sample, which is what was expected. This fact indicates that we can have informations for the temporal evolution of the water diffusion process. This also means that one can know if the peak detected is due to moisture or is a permanent defect by heating the desirable area. If the peak disappears then it is water.

As a last part of this work, we tried to create a more realistic situation, using a painted gypsum slab (Figure 47 (a)), in which we added water from the backside, in a way that the paint layer remained dry. Then we took measurements while the sample was drying on air. The gypsum slab was 1.17 mm thick and the paint we used was yellow tempera.

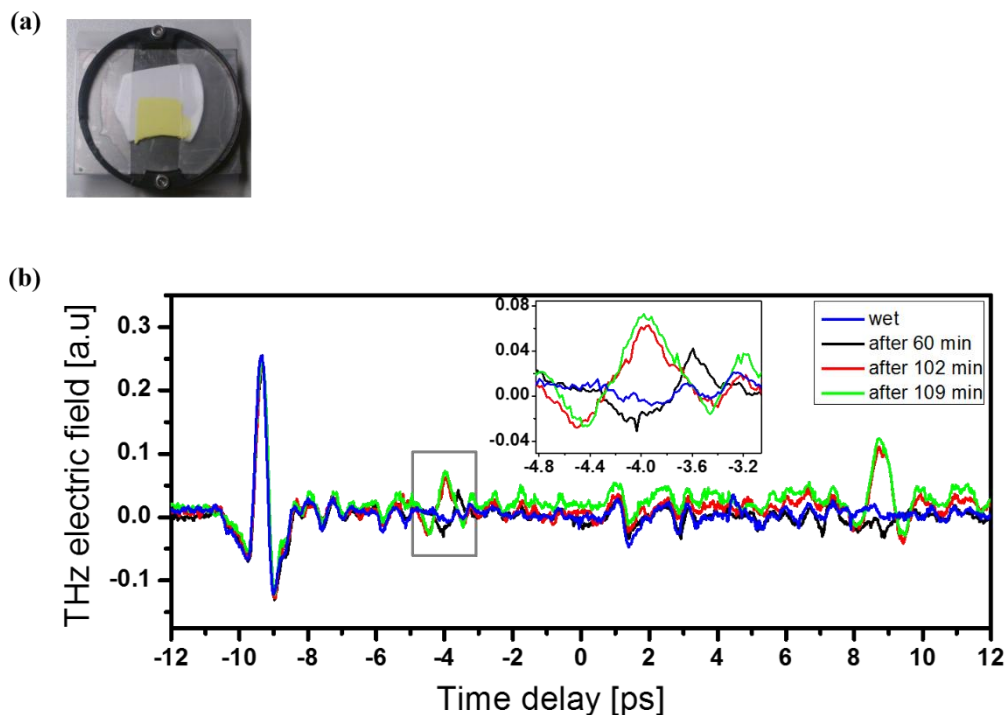


Figure 47: (a) painted gypsum slab and corresponding THz electric fields as the sample dries in air (b).

In the electric fields of Figure 47 (b) for the first measurement when gypsum is fully wet, there is just one peak from the air-paint interface ( $t_1=-9.3$  ps). As the gypsum slab slowly dries, two more peaks appear, the second one from paint-gypsum interface ( $t_2=-4$  ps) and the third one from the gypsum-metal (holder) interface ( $t_3=8.7$  ps).

Summarizing, in this chapter a first effort to detect indepth moisture in gypsum samples was made. In our experiments we managed to detect the interface between dry and wet sample, so knowing the position of the reflected peak one can detect the exact position of the interface, thus we can know where the moisture front is located. We also can have an image of the temporal evolution of the moisture in our sample by recording the change of the peak's amplitude. The decrease of the peak means that water penetrates more in the dry region of the sample. This change in the peak's amplitude is also an indication that the reflection comes from the interface

between dry and wet area and not from a permanent defect. In this case nothing should change.

## **Conclusions – Perspectives**

In this thesis, was presented a first attempt towards the detection and localization of moisture in depth of some millimeters, exploiting THz radiation through a THz-TDS reflection system, using an experimental routine and the appropriate analysis. Our homemade reflection THz-TDS system was presented and its ability to distinguish different moisture contents for paper samples, with single surface and stratified ones, was demonstrated. Furthermore, gypsum, a material commonly found in walls, was found to be the most suitable one for our experiments among a number of different materials that was tested. Finally, in the last part of this thesis, the ability to distinguish the presence and the specific location of moisture inside a sample was demonstrated both experimentally and theoretically. Further research should be done by applying this technique in an even more realistic environment. Further information could be extracted looking at the phase and the spectrum of the THz electric field using more sophisticated algorithms for the analysis.

## References

- 1 W. Zouaghi, M. D. Thomson, K. Rabia, R. Hahn, V. Blank, and H. G. Roskos, *European Journal of Physics* **34**, S179 (2013).
- 2 J. A. Hejase, P. R. Paladhi, and P. Chahal, *Components, Packaging and Manufacturing Technology*, *IEEE Transactions on* **1**, 1685 (2011).
- 3 J. P. Guillet, B. Recur, L. Frederique, B. Bousquet, L. Canioni, I. Manek-Hönniger, P. Desbarats, and P. Mounaix, *J Infrared Milli Terahz Waves* **35**, 382 (2014).
- 4 C. Jansen, et al., *Applied Optics* **49**, E48 (2010).
- 5 H. Kao-Cheng and W. Zhaocheng, *Microwave Magazine*, *IEEE* **12**, 108 (2011).
- 6 S. Ishii, M. Seta, N. Nakai, S. Nagai, N. Miyagawa, A. Yamauchi, H. Motoyama, and M. Taguchi, *Polar Science* **3**, 213 (2010).
- 7 I. C. Mayorga, A. Schmitz, T. Klein, C. Leinz, and R. Gusten, *Terahertz Science and Technology*, *IEEE Transactions on* **2**, 393 (2012).
- 8 T. Ouchi, K. Kajiki, T. Koizumi, T. Itsuji, Y. Koyama, R. Sekiguchi, O. Kubota, and K. Kawase, *J Infrared Milli Terahz Waves* **35**, 118 (2014).
- 9 G. J. Wilmink, et al., *Lasers in Surgery and Medicine* **43**, 152 (2011).
- 10 Z. D. Taylor, et al., *Terahertz Science and Technology*, *IEEE Transactions on* **1**, 201 (2011).
- 11 H. Wu and M. Khan, *Journal of Molecular Structure* **1020**, 112 (2012).
- 12 Y.-C. Shen, *International Journal of Pharmaceutics* **417**, 48 (2011).
- 13 S. Yao-chun and P. F. Taday, *Selected Topics in Quantum Electronics*, *IEEE Journal of* **14**, 407 (2008).
- 14 H.-B. Liu, Y. Chen, and X. C. Zhang, *Journal of Pharmaceutical Sciences* **96**, 927 (2007).
- 15 U. Kaatze, *Measurement Science and Technology* **24**, 012005 (2013).
- 16 M. Naftaly and R. E. Miles, *Proceedings of the IEEE* **95**, 1658 (2007).
- 17 A. I. McIntosh, B. Yang, S. M. Goldup, M. Watkinson, and R. S. Donnan, *Chemical Society Reviews* **41**, 2072 (2012).
- 18 L. Hai-Bo, Z. Hua, N. Karpowicz, C. Yunqing, and Z. Xi-Cheng, *Proceedings of the IEEE* **95**, 1514 (2007).
- 19 F. F. John, S. Brian, H. Feng, G. Dale, B. Robert, O. Filipe, and Z. David, *Semiconductor Science and Technology* **20**, S266 (2005).
- 20 A. S. Skryl, J. B. Jackson, M. I. Bakunov, M. Menu, and G. A. Mourou, *Applied Optics* **53**, 1033 (2014).
- 21 P. Mounaix, A. Younus, J. C. Delagnes, E. Abraham, L. Canioni, and M. Fabre, *J. Eur. Opt. Soc.-Rapid Publ.* **6** (2011).
- 22 K. Fukunaga, Y. Ogawa, S. i. Hayashi, and I. Hosako, *IEICE Electronics Express* **4**, 258 (2007).

- 23 J. W. B. Gillian C. Walker, Wendy Matthews, Soumali Roychowdhury, Julien Labaune, Gerard Mourou, Michel Menu, Ian Hodder, and J. Bianca Jackson, *Optical Society of America* **21** (2013).
- 24 G. Filippidis, M. Massaouti, A. Selimis, E. Gualda, J. M. Manceau, and S. Tzortzakis, *Applied Physics A: Materials Science & Processing* **106**, 257 (2012).
- 25 A. Redo-Sanchez, G. Salvatella, R. Galceran, E. Roldos, J.-A. Garcia-Reguero, M. Castellari, and J. Tejada, *Analyst* **136**, 1733 (2011).
- 26 C. D. Maria Massaouti, Andrei Gorodetsky, Anastasios D. Koulouklidis, Stelios Tzortzakisa, *Applied Spectroscopy Reviews* **67** (2013).
- 27 C. Jördens and M. Koch, *Optical Engineering* **47**, 037003 (2008).
- 28 C. Wai Lam, D. Jason, and M. M. Daniel, *Reports on Progress in Physics* **70**, 1325 (2007).
- 29 M. R. Leahy-Hoppa, M. J. Fitch, X. Zheng, L. M. Hayden, and R. Osiander, *Chemical Physics Letters* **434**, 227 (2007).
- 30 R. K. May, M. J. Evans, S. Zhong, I. Warr, L. F. Gladden, Y. Shen, and J. A. Zeitler, *Journal of Pharmaceutical Sciences* **100**, 1535 (2011).
- 31 T. Sakamoto, A. Portieri, D. Arnone, P. Taday, T. Kawanishi, and Y. Hiyama, *J Pharm Innov* **7**, 87 (2012).
- 32 J. Hisazumi, T. Suzuki, N. Wakiyama, H. Nakagami, and K. Terada, *Chemical and Pharmaceutical Bulletin* **60**, 831 (2012).
- 33 G. J. Wilmink, B. L. Ibey, C. L. Roth, R. L. Vincelette, B. D. Rivest, C. B. Horn, J. Bernhard, D. Roberson, and W. P. Roach, 2010), p. 75620K.
- 34 P. C. Ashworth, E. Pickwell-MacPherson, E. Provenzano, S. E. Pinder, A. D. Purushotham, M. Pepper, and V. P. Wallace, *Optics Express* **17**, 12444 (2009).
- 35 A. M. Hassan, D. C. Hufnagle, M. El-Shenawee, and G. E. Pacey, in *Microwave Symposium Digest (MTT), 2012 IEEE MTT-S International*, 2012), p. 1.
- 36 M. W. Ruth, E. C. Bryan, P. W. Vincent, J. P. Richard, D. A. Donald, H. L. Edmund, and P. Michael, *Physics in Medicine and Biology* **47**, 3853 (2002).
- 37 R. M. Woodward, V. P. Wallace, D. D. Arnone, E. H. Linfield, and M. Pepper, *Journal of Biological Physics* **29**, 257 (2003).
- 38 D. Crawley, C. Longbottom, V. P. Wallace, B. Cole, D. Arnone, and M. Pepper, *Journal of Biomedical Optics* **8**, 303 (2003).
- 39 D. Banerjee, W. von Spiegel, M. D. Thomson, S. Schabel, and H. G. Roskos, *Opt. Express* **16**, 9060 (2008).
- 40 S. Tanaka, Y. Fujiwara, Y. Fujii, S. Okumura, H. Togo, N. Kukutsu, and S. Mochizuki, *J Wood Sci* **59**, 375 (2013).
- 41 R. P. C. J. S. W. D. M. M. K. T. Kürner, *Infrared Milli Waves* (2007).
- 42 Y. Oyama, L. Zhen, T. Tanabe, and M. Kagaya, *NDT & E International* **42**, 28 (2009).
- 43 F. Ospald, et al., *Optical Engineering* **53**, 031208 (2013).
- 44 K. Fukunaga and M. Picollo, *Applied Physics A: Materials Science & Processing* **100**, 591 (2010).

- 45 M. S. Sherwin, in *CLEO: 2013* (Optical Society of America, San Jose, California, 2013),  
p. JF1K.1.
- 46 M. Ho<sup>®</sup>mann, Phd Thesis (2006).
- 47 S. L. Dexheimer, Book (2008).
- 48 J. X. X.-C. Zhang, Book (2010).
- 49 T. I. Oh, Y. S. You, and K. Y. Kim, *Optics Express* **20**, 19778 (2012).
- 50 B. Clough, J. Dai, and X.-C. Zhang, *Materials Today* **15**, 50 (2012).
- 51 S. Casalbuoni, H. Schlarb, B. Schmidt, P. Schmäuser, B. Steffen, and A. Winter, *Physical  
Review Special Topics - Accelerators and Beams* **11**, 072802 (2008).
- 52 M. Massaouti, J. M. Manceau, A. Selimis, and S. Tzortzakos, *Journal of Molecular  
Structure* **1006**, 28 (2011).
- 53 Y. Shen, T. Watanabe, D. A. Arena, C. C. Kao, J. B. Murphy, T. Y. Tsang, X. J. Wang,  
and G. L. Carr, *Physical Review Letters* **99**, 043901 (2007).
- 54 D. J. Cook and R. M. Hochstrasser, *Opt. Lett.* **25**, 1210 (2000).
- 55 H. G. Roskos, M. D. Thomson, M. Kreß, and T. Löffler, *Laser & Photonics Reviews* **1**,  
349 (2007).
- 56 X. Xie, J. Dai, and X. C. Zhang, *Physical Review Letters* **96**, 075005 (2006).
- 57 K.-Y. Kim, J. H. Glowina, A. J. Taylor, and G. Rodriguez, *Opt. Express* **15**, 4577 (2007).
- 58 J.-M. Manceau, Phd Thesis (2010).
- 59 P. U. Jepsen and B. Fischer, *Optics Letters* **30**, 29 (2005).
- 60 D. Capitani, N. Proietti, M. Gobbino, L. Soroldoni, U. Casellato, M. Valentini, and E.  
Rosina, *Analytical and Bioanalytical Chemistry* **395**, 2245 (2009).
- 61 R. Olmi, M. Bini, A. Ignesti, S. Priori, C. Riminesi, and A. Felici, *Measurement Science  
and Technology* **17**, 2281 (2006).
- 62 K. Udo and H. Christof, *Measurement Science and Technology* **21**, 082001 (2010).
- 63 J. B. Jackson, M. Mourou, J. Labaune, J. F. Whitaker, I. I. N. Duling, S. L. Williamson,  
C. Lavier, M. Menu, and G. A. Mourou, *Measurement Science and Technology* **20**,  
075502 (2009).
- 64 M. Koch, S. Hunsche, P. Schumacher, M. C. Nuss, J. Feldmann, and J. Fromm, *Wood  
Sci. Technol.* **32**, 421 (1998).
- 65 S. Tanaka, K. Shiraga, Y. Ogawa, Y. Fujii, and S. Okumura, *J Wood Sci*, 1 (2014).
- 66 M. Reid and R. Fedosejevs, *Applied Optics* **45**, 2766 (2006).
- 67 A. Teti, D. Rodriguez, J. Federici, and C. Brisson, *J Infrared Milli Terahz Waves* **32**, 513  
(2011).
- 68 Y. L. Hor, J. F. Federici, and R. L. Wample, *Applied Optics* **47**, 72 (2008).
- 69 S. Mukherjee, J. Federici, P. Lopes, and M. Cabral, *J Infrared Milli Terahz Waves* **34**,  
539 (2013).
- 70 Y. S. Jin, G. J. Kim, and S. G. Jeon, *J. Korean Phys. Soc.* **49**, 513 (2006).
- 71 J. H. P. C. Jelena Obradovic , Ole Hirsch , Michael D. Mantle ,Michael L. Johns , Lynn  
F. Gladden *Polymer* **48** (2007).

- <sup>72</sup> S. Wietzke, C. Jansen, M. Reuter, T. Jung, D. Kraft, S. Chatterjee, B. M. Fischer, and M. Koch, *Journal of Molecular Structure* **1006**, 41 (2011).
- <sup>73</sup> J. Balakrishnan, B. M. Fischer, and D. Abbott, *Applied Optics* **48**, 2262 (2009).
- <sup>74</sup> A. J. Gatesman, A. Danylov, T. M. Goyette, J. C. Dickinson, R. H. Giles, W. Goodhue, J. Waldman, W. E. Nixon, and W. Hoen, 2006), p. 62120E.
- <sup>75</sup> T. Hattori, H. Kumon, and H. Tamazumi, in *Infrared Millimeter and Terahertz Waves (IRMMW-THz), 2010 35th International Conference on*, 2010), p. 1.
- <sup>76</sup> P. Mousavi, F. Haran, D. Jez, F. Santosa, and J. S. Dodge, *Applied Optics* **48**, 6541 (2009).
- <sup>77</sup> J. Dash, S. Ray, K. Nallappan, S. Sasmal, and B. Pesala, 2014), p. 89850Q.
- <sup>78</sup> G. C. Walker, J. B. Jackson, D. Giovannacci, J. W. Bowen, B. Delandes, J. Labaune, G. Mourou, M. Menu, and V. Detalle, 2013), p. 87900H.
- <sup>79</sup> J. B. Jackson, M. Mourou, J. F. Whitaker, I. N. Duling Iii, S. L. Williamson, M. Menu, and G. A. Mourou, *Optics Communications* **281**, 527 (2008).